

**UCSF**

**UC San Francisco Electronic Theses and Dissertations**

**Title**

In vitro Reconstitution of DNA Segregation; A Plasmid Spindle Driven by a Dynamically Unstable Actin Homologue

**Permalink**

<https://escholarship.org/uc/item/0cf8863m>

**Author**

Garner, Ethan Clark

**Publication Date**

2007-05-15

Peer reviewed|Thesis/dissertation

In vitro Reconstitution of DNA Segregation;  
A Plasmid Spindle Driven by a Dynamically Unstable Actin Homologue

by

Ethan Clark Garner

DISSERTATION

Submitted in partial satisfaction of the requirements for the degree of

DOCTOR OF PHILOSOPHY

in

Biochemistry

in the

GRADUATE DIVISION

of the

UNIVERSITY OF CALIFORNIA, SAN FRANCISCO



## Acknowledgements

I would like to thank Dyche, for his advice, teachings, inspiration, and the limitless amount of freedom he has provided to all of us within the lab.

I would like to thank Chris Campbell for being my partner in this story, and for providing the calm counterweight to my random fury.

I would like to thank the Mullins Lab for their advice, support, criticism, and for making the lab environment an intellectually stimulating and fun place to work. I am also quite indebted to the Vale lab, as their expertise and support has made this work possible.

Other mentors have also been incredibly helpful over the last ten years. Ron Vale, Clare Waterman-Storer, and Tim Mitchison, and Keith Dunker have all enriched my life.

I would like to thank all of the collaborators I have met through the years; Hernan Garcia, John Alberts, Lea Trichet, Doug Weibel, Adam Douglass, and Nico Sturman. These people have enriched my thinking and approaches.

I would like to thank the random walk of life for having me end up in the place and position I am, and the random occurrence of luck for this project working out so well.

Finally, I would like to thank Quincey Justman for enriching my life in personal, spiritual, and scientific ways beyond anything I could ever have imagined.



***In vitro* Reconstitution of DNA Segregation;  
A Plasmid Spindle Driven by a Dynamically Unstable Actin Homologue**

Ethan Clark Garner

**Abstract**

The *par* operon of the R1 plasmid constructs a DNA segregating spindle from three components, *parC*, ParR, and ParM. *parC* is a centromeric stretch of DNA which is bound by the protein ParR. ParM is an actin homologue that polymerizes into two stranded filaments that can interact with the ParR/*parC* complex. These three components are both necessary and sufficient to segregate *parC* containing plasmids, implying that the *par* operon is a biochemically self-contained DNA segregation apparatus. To elucidate how this system functions to segregate plasmid DNA, we wished to determine the intrinsic kinetic properties of ParM assembly, and how this assembly is regulated by the interaction with its cargo, the ParR/*parC* complex.

We find that ParM displays three properties that distinguish its assembly from that of eukaryotic actins. 1) ParM displays hydrolysis dependent dynamic instability, the stochastic switching between states of growth and rapid depolymerization. 2) ParM filaments display a very rapid rate of nucleation, occurring at a rate 200-fold faster than actin. 3) ParM filaments exhibit no kinetic polarity, with equal rates of growth at each filament end.

By combining ParM with bead immobilized ParR/*parC* we demonstrate that these three components can create bipolar spindles *in vitro* similar to those observed *in vivo*. ParR/*parC* coated microspheres are connected by bundles of ParM filaments that elongate over time, pushing the microspheres apart over long distances. Speckle microscopy and photobleaching experiments demonstrate that this motility is driven by insertional polymerization at the bead surface. We find that the ParR/*parC* complex prevents ParM filament ends from catastrophe by stabilizing filaments down to the ATP-ParM critical concentration. Furthermore, we show that the dynamic instability of ParM is critical to the spatial regulation of the R1 spindle, as filament ends that are not bound at each end by ParR/*parC* are destined to undergo catastrophe. The dynamic instability of ParM also provides an energetic differential to power spindle elongation, as the turnover of background, unbound filaments provide the monomer excess required for the growth of stabilized, spindle associated filaments.

---

R. Dyche Mullins

Advisor and Committee Chairman



## Contributions

Much of this work was done in collaboration with a number of people both within the lab and outside the lab. The work within Chapter 3 was done as a joint effort between Chris Campbell and I, and the first authorship is shared equally for that publication.

Chapters 4 and 5 detail the reconstituted *par* system, and this work was carried out in collaboration with many others. Doug Weibel made the microfabriated PDMS chambers in Chapter 4. Chris Campbell did the negative stain electron micrographs of R1 spindles in chapter 4. The *parC* coated oil droplets in described in Chapter 5 were made by Lea Trichet. Members of within Rudolph Oldenburg's lab at Woods Hole carried out the polarization microscopy shown in Chapter 5.

## Table of Contents

<b>Preface</b>	Copyright	ii
	Acknowledgements	iii
	Abstract	iv
	Contributions	vi
	Table of Contents	vii
	List of Tables	viii
	List of Figures	ix
<b>Chapter 1</b>	Introduction	1
<b>Chapter 2</b>	Background	10
<b>Chapter 3</b>	Dynamic Instability in a Prokaryotic Actin Homologue	21
<b>Chapter 4</b>	Reconstitution of DNA Segregation Driven by Assembly of a Prokaryotic Actin Homolog	71
<b>Chapter 5</b>	Unpublished Experiments	109
<b>Appendix A</b>	Permissions	131

## List of Tables

### **Chapter 3.**

Table 1: Kinetic Parameters of ParM and Actin.	44
--	----

## List of Figures

### **Chapter 3**

Figure 1:	35
Figure 2:	36
Figure 3:	37
Figure 4:	38
Supplementary Figure 1:	53
Supplementary Figure 2:	54
Supplementary Figure 3:	55
Supplementary Figure 4:	56

### **Chapter 4**

Figure 1:	82
Figure 2:	83
Figure 3:	84
Figure 4:	85
Supplementary Figure 1:	93
Supplementary Figure 2:	93
Supplementary Figure 3:	94
Supplementary Figure 4:	94
Supplementary Figure 5:	95
Supplementary Figure 6:	95

Supplementary Figure 7:	96
Supplementary Figure 8:	97

## **Chapter 5**

Figure 1:	119
Figure 2:	120
Figure 3:	121
Figure 4:	122
Figure 5:	123
Figure 6:	124



# **Chapter 1**

## **Introduction**

## **Bacterial cytoskeletal systems.**

From the advent of light microscopy, eukaryotic cells have been observed to contain a number of spatially distinct intracellular domains. These internal regions allow the cell to localize critical functions and compartmentalize linked sets of chemical reactions. In order to impart this higher order structure, eukaryotes have evolved a series of self-assembling polymers that serve as dynamic scaffolds for the organization and trafficking of cellular factors. As cells regulate both the assembly and disassembly of these structural elements, cells can then harness the polymerization dynamics of these fibers to carry out work.

As bacteria are only 5 fold wider (1 $\mu$ m) than the resolution limit of light microscopy (0.2 $\mu$ m) any internal organization of the prokaryotic cytoplasm remained unobservable for many years. Although bacteria display a wide range of external morphologies, they were assumed to be internally homogeneous mixtures of cellular components. This view was reinforced by the lack of observable cytoskeletal filaments, as such structures might, by analogy to eukaryotes, be required to organize the cellular volume.

This simple “bag of reactions” paradigm led to a conceptual framework that explained away many cellular tasks through passive processes. DNA segregation into daughter cells could be achieved by simply anchoring of each origin opposing poles, and as the bacterium elongated the DNA would be pulled apart as a passive entity (*1*). Cell division

was also justified in a passive sense; by analogy to the physics of soap bubbles, Koch explained that once the bacterium reached a length that was energetically unfavorable, the cell wall would bend inward, initiating cell division (2).

The development of gold conjugated antibodies and GFP fusions very rapidly began to draw the concept of a passive, homogeneous cytoplasm into question. Immuno-gold electron microscopy demonstrated that the chemoreceptors of *E. coli* were localized to the poles of the cell (3). Fusions of GFP to components of the replisome showed that the DNA replication machinery was localized at the midcell (4). During the asymmetric process of *B. subtilis* sporulation, a series of sporulation factors were found to localize to various subcellular locales in a temporal sequence. Within the 2-stage cell cycle of *C. crescentus* a number of proteins also localize to subcellular positions in a cell-cycle dependent manner (for reviews see (5, 6)).

The specific localization of these cellular factors dictates that bacterial cells contain mechanisms to both establish and target these cellular regions. By analogy to eukaryotes, these processes may involve self-assembling filaments. Eukaryotes utilize the microtubule cytoskeleton to establish a radial array upon which the cell is organized, and utilize both the actin and microtubule cytoskeletons as scaffolds to organize the cellular components.

When components of the prokaryotic cytoskeleton were discovered, it was striking that they were structural homologues of their eukaryotic counterparts. Work by Bi and

Lutkenhaus (7) demonstrated that the essential FtsZ protein localized in a ring at the point of cell division, leading them to postulate that FtsZ could self assemble into a cytoskeletal structure. This hypothesis was verified by electron microscopy, showing that purified FtsZ assembles in a GTP dependent manner into filamentous structures (8). These results, as well as the presence of a PROSITE tubulin sequence motif (9), led to the hypothesis that FtsZ was a homologue of eukaryotic tubulin, a hypothesis verified by the structure of FtsZ (10). This structure demonstrated that while the sequence of FtsZ is divergent from tubulin, the overall fold and secondary structure is quite similar.

The discovery of a prokaryotic actin homologue occurred a few years later. Jones et al. demonstrated that the MreB family of actin-like proteins form helical structures beneath the cell membrane in *B. subtilis* (11). These proteins control the formation the rod shape of the bacterium, as deletions or reductions in these genes lead to morphological defects. Shortly afterward, the crystal structure of a thermophilic MreB was solved (12), verifying that this family of proteins are structural analogs of eukaryotic actin. Similar to eukaryotic actins these proteins also assemble into filaments in a ATP and  $Mg^{2+}$  dependent manner.

Although prokaryotes contain structural homologues of eukaryotic polymers, the exact function of these self-assembling filaments is still not fully understood. Unlike their eukaryotic counterparts, there has been no direct evidence that prokaryotic cells harness the polymerization dynamics of these proteins to exert force. Rather it appears that these

polymers function as scaffolds to localize various components and give the cell internal directional cues.

While it has been proposed that multiple transitions between FtsZ-GTP to FtsZ-GDP filaments could power cell division (13), there has been little evidence for this hypothesis. Using a combination of mutants and GFP fusions of divisome components, several groups were able to determine the order by which the bacterial division apparatus assembles at the midcell (for a review see (14)). In all cases, FtsZ is the first protein to arrive, suggesting that the FtsZ cytoskeleton serves as a positional scaffold to localize the necessary components of the division machinery at the midcell.

The cellular roles for prokaryotic actins are still, as of yet, poorly defined. The initial observation that depletion of MreB led to cell shape defects suggested that this protein directs the establishment and maintenance of the peptidoglycan sacculus (11). This linkage has been elucidated by Carbello-lopez (15), who demonstrated that MreBH associates with the cell wall hydrolyase LytE in *B. subtilis*.

Aside from the maintenance of shape, MreB appears to be involved in many other processes involving the localization of proteins either to positions along the cell length or to the poles of the cell. MreB was one of the first proteins shown to localize in a spiral pattern along the length of the cell (11). As other proteins have also been visualized in similar spiral structures, it has been assumed that these factors associate with MreB.

Although a few of these proteins do indeed require MreB for spiral localization (16, 17), other proteins appear to form spirals independently or in opposition to MreB (18).

Following these two initial discoveries, a series of other prokaryotic cytoskeletal elements have been identified, all of which appear to be evolutionary divergent from each other. The ParM family of proteins are distant actin homologues that build minimal mitotic spindles to segregate low copy plasmids in gram negative bacteria (19). AlfA, a protein evolutionarily distant from ParM, functions to accomplish a similar task in *B. subtilis*. (20) MamK is another actin homologue involved in the positioning of magnetite rich organelles within the magnetotactic bacterium *M. magneticum* (21, 22).

In order to convert polymerization into useful work or positional information, cells need to regulate the assembly of these polymers. Eukaryotic actins and tubulins interact with hundreds of cellular components (23, 24), affecting both the polymerization kinetics and filament superstructure. Similar to their eukaryotic homologues the prokaryotic cytoskeleton is likely to both interact with and be regulated by numerous cellular factors.

The intent of this thesis was to determine both the intrinsic and emergent kinetic properties of a bacterial polymer system. As biological polymers exist within networks of interacting partners that affect both the assembly kinetics and cellular functions, the biological behavior of a polymer may not be realized when the protein is studied alone.

The chromosomally encoded prokaryotic actin and tubulin homologues, MreB and FtsZ, most likely interact with many other proteins which remain unidentified. The possibility of multiple interactions would likely complicate a complete reconstitution of these systems, as the biochemical complexity of the system will scale with the number of components. Rather, in order to elucidate a polymer system in detail, I chose to study the most minimal and self-contained bacterial polymer system available. Of all known systems, the type II plasmid segregation apparatuses appear eminently tractable, as they contain only three components. The different type II systems can be quite evolutionarily divergent, but each contains a common set of factors: 1) a DNA element with multiple protein binding motifs, 2) an actin-homologue that polymerizes into actin like filaments, and 3) an adapter protein, that binds to both the repeats in the DNA and the polymerized actin-homologue filaments.

1. F. Jacob, A. Ryter, and F. Cuzin, *Cold Spring Harbor Symp. Quant. Biol* **28**, 329 (1963).
2. A. L. Koch, *Bacterial growth and form*. (Chapman & Hall, Inc., New York, NY, 1993), pp.
3. J. Maddock, L. Shapiro, *Science* **259**, 1717 (1993).
4. K. Lemon, A. Grossman, *Science (New York, N.Y.)* **282**, 1516 (Nov, 1998).
5. L. Shapiro, D. Kaiser, R. Losick, *Cell* **73**, 835 (Jun, 1993).
6. L. Shapiro, R. Losick, *Science (New York, N.Y.)* **276**, 712 (May, 1997).
7. E. Bi, J. Lutkenhaus, *Nature* **354**, 161 (1991).
8. A. Mukherjee, J. Lutkenhaus, *J Bacteriol* **176**, 2754 (1994).

9. H. Erickson, *Cell* **80**, 367 (Feb, 1995).
10. J. Lowe, L. Amos, *Nature* **391**, 203 (1998).
11. L. Jones, R. Carballido-López, J. Errington, *Cell* **104**, 913 (Apr, 2001).
12. F. van den Ent, L. Amos, J. Lowe, *Nature* **413**, 39 (2001).
13. H. Erickson, *Current opinion in cell biology* **13**, 55 (Feb, 2001).
14. J. Errington, R. Daniel, D. Scheffers, *Microbiology and molecular biology reviews: MMBR* **67**, 52 (Mar, 2003).
15. R. Carballido-López *et al.*, *Developmental cell* **11**, 399 (Sep, 2006).
16. D. Shiomi, M. Yoshimoto, M. Homma, I. Kawagishi, *Molecular microbiology* **60**, 894 (May, 2006).
17. R. Figge, A. Divakaruni, J. Gober, *Molecular microbiology* **51**, 1321 (Feb, 2004).
18. N. Dye, Z. Pincus, J. Theriot, L. Shapiro, Z. Gitai, *Proceedings of the National Academy of Sciences of the United States of America* **102**, 18608 (Dec, 2005).
19. J. Moller-Jensen, R. Jensen, J. Lowe, K. Gerdes, *Embo J* **21**, 3119 (2002).
20. E. Becker *et al.*, *The EMBO journal* **25**, 5919 (Dec, 2006).
21. N. Pradel *et al.*, *Biochemical and biophysical research communications* **353**, 493 (Dec, 2006).
22. A. Komeili, Z. Li, D. Newman, G. Jensen, *Science (New York, N.Y.)* **311**, 242 (Dec, 2005).
23. T. Pollard, L. Blanchoin, R. Mullins, *Annual review of biophysics and biomolecular structure* **29**, 545 (Aug, 2000).
24. T. Pollard, G. Borisy, *Cell* **112**, 453 (2003).



## **Chapter 2**

### **Background**

## The *par* segregation machinery of the R1 plasmid

Low copy plasmids are large (>100kb), extra chromosomal DNA elements found in prokaryotes. These plasmids contain many actively transcribed genes, including factors involved in conjugation, protection from heavy metal toxicity, and antibiotic resistance. Because of their size and transcriptional load, these plasmids impose a significant metabolic burden to their hosts, and hence are limited to a few copies per cell (1, 2). The retention of these plasmids in bacterial populations is ensured by several mechanisms, including the active, polymerization driven segregation apparatus encoded by *par* operons within the plasmids. These operons always contain three elements: a centromeric DNA sequence, a DNA binding protein, and an ATPase. Phylogenetic analysis of the ATPase genes within these operons indicate that these partitioning cassettes fall into two families: 1) Those that contain Walker box ATPases (Type I segregation systems), and 2) those that contain actin-like ATPases (Type II segregation systems) (3). The phylogeny of these two classes correlate with plasmid incompatibility groups, suggesting that the mechanisms of segregation are different between classes but, within each class, are similar enough that they can compete with each other during the plasmid segregation process (3).

The plasmid R1 *par* operon encodes a gene called ParM that falls into the type II actin-like family of partitioning genes. This 100kb plasmid was originally isolated in the 1950s from *S. flexneri* in Japan (4). Work by Gerdes and Molin demonstrated that the *par* region responsible for plasmid stabilization maps to a 1.5 Kb region of DNA. This

sequence, when placed into a low copy mini-F plasmid stabilized the plasmid 100 fold (5).

Sequencing of this fragment indicated that the *par* operon contained two proteins, ParM (36kd) and ParR (13.3kd) (5). Upstream of these two sequences is a small region termed *parC* that contains 2 sets of 5 direct sequence repeats flanking the *par* promoter (6).

Deletion of any of these three components (ParM, ParR or *parC*) leads to a loss of plasmid stabilization. Furthermore, stabilization of a *parC* containing plasmid can be accomplished by donation of ParM or ParR *in trans* (6). These results demonstrate that these three components are both necessary and sufficient for plasmid stabilization.

When extra copies of *parC* are introduced into the cell on other plasmids this leads to destabilization of the R1 plasmid. This led Dam and Gerdes to suggest that the *parC* region functions as a centromeric region for plasmid segregation (6). Computational approaches and anomalous migration upon DNA gels suggests that the *parC* region is curved (7), similar to eukaryotic centromeres. ParR has been shown to bind to *parC* by the use of gel shifts and surface plasmon resonance assays (8). Electron microscopy studies have also shown that ParR protein binds to *parC*. Strikingly, ParR binding to *parC* shortens the contour length of the DNA by 130bp, exactly the length of the *parC* region (9). This suggests that the *parC* repeats bind to ParR in a manner similar to eukaryotic histones, with the *ParC* DNA wrapping around a complex of ParR molecules. This work also suggested that the ParR protein could assist in pairing 2 *parC* containing strands in a head to tail orientation, a paring that could be enhanced in the presence of

both ParM and ATP. Although the paring of *parC* by ParM and ParR is a novel result, this thread of experimentation appears to have stalled, leaving the role of plasmid paring in R1 segregation an unresolved question.

The fact that the ParR binding sites flank the *par* promoter suggested that ParR binding could have a regulatory effect on transcription from the *par* operon. Modulation of the cellular level of ParR did indeed show that this operon was negatively self regulated. Using primer extension from total mRNA as well as LacZ fusions, it was shown that deletions of ParR led to greater expression of genes driven by the *par* promoter, while overexpression of ParR decreased transcription in a titratable manner (10).

The multiple sequence repeats within *parC* are critical to both the transcriptional regulation and the centromeric function of the ParR/*parC* complex. Deletion of individual *parC* repeats decreases ParR mediated repression and also decreases the stabilization of *par* containing plasmids. Deletion of 5 of the repeats on one side of the promoter reduces ParR mediated repression 10 fold, and reduces plasmid stabilization 22-35 fold. Deletion of only 2 repeats decreases repression 5-10 fold and decreases plasmid stabilization by 2-5 fold (11).

The effect of the number of *parC* repeats on the *in vivo* functions can be explained by the relationship of the number of sequence repeats within *parC* to the affinity and cooperativity of ParR binding. Gels shifts demonstrate a tight and cooperative binding of ParR to full length *parC*, as ParR binds to all 10 repeats with an apparent Kd of 40nM

and a hill coefficient of 3 (8). As the number of sequence repeats within *parC* are reduced, the affinity and cooperativity of ParR binding decreases: no binding is observed of ParR to a single repeat and weaker binding ( $K_d$  between 80-800nm) is observed with only two or three repeats. ParR is a dimer in solution, as demonstrated by gel filtration, sedimentation analysis (8), yeast-2-hybrid assays (12), and chemical crosslinking (13). It appears that each sequence repeat within *parC* is bound by each ParR dimer, as the number of intermediate bands in gel shift experiments can be correlated to the number of *parC* repeats (8). The synthesis of the above genetic and biochemical data suggest that the number of sequence repeats within *parC* affect the cooperativity and affinity of ParR binding to *parC*, and this change in binding affinity then affects the formation of a centromeric and repressive ParR/*parC* complex.

The third component of the *par* operon is the force generating component, ParM. Initial localization experiments utilizing GFP-ParM fusions indicated that ParM colocalized with the *parC* containing plasmids at discrete foci within the cell (14). This result appears to be an artifact of expressing 100% GFP-ParM, as later work using immunofluorescence against native protein demonstrated ParM filaments that extend the length of the cell (15). These filaments are present in approximately 30% of the cells, and filament formation requires the presence of both ParR and *parC*. Later efforts tracked the localization of *parC* plasmids simultaneously with ParM filaments, indicating that ParM filaments within the cell frequently have a plasmid located at each end of the filament (8). Elegant experiments controlling the copy number of the plasmids demonstrated that ParM spindle formation requires at least 2 plasmids in the cell. Plasmids held under

replication arrest contained only one plasmid, and no visible ParM spindles. However, once the plasmids were released from replication arrest ParM filaments were detectable in the majority of the cells. These results suggested the exciting possibility that ParM, ParR, and *parC* form a minimal, bipolar mitotic spindle that segregate plasmids to the opposing poles of the cell.

ParM had been noted to contain sequence motifs that were indicative of proteins that exhibit an actin fold, such as HSP70, MreB and eukaryotic actins (16). The crystal structures of nucleotide-free and ADP-bound ParM were later solved, demonstrating a conservation of the ATP binding pocket, and moderate conservation of the secondary structure between ParM and actin (17). The fact that ParM can form a DNA segregating spindle is striking, as ParM is an actin homologue while all eukaryotic spindles are composed of tubulins.

Like many actin family proteins, ParM has been shown to exhibit ATPase activity (12). Following the realization that ParM may polymerize into filaments *in vivo*, it was shown by electron microscopy that ParM can polymerize into 2-stranded, helical filaments *in vitro* in an ATP and  $Mg^{2+}$  dependent manner similar to eukaryotic actin (15, 17).

ParM has been shown to polymerize in solution through the use of light scattering assays. Polymerization signal could only be observed when ParM was above 5 $\mu$ M, but not when ParM was at 1 $\mu$ M, implying the presence of a critical concentration for ParM assembly (15). One notable result from these experiments is that the polymerization of ParM is

incredibly rapid, as the polymerization signal appeared to reach its maxima in a matter of seconds. This fast polymerization at all concentrations is in contrast to eukaryotic actins, which exhibit a very slow rate of nucleation.

Another feature that differentiates ParM assembly from that of eukaryotic actin is the fact that the filaments are not less stable when bound to ADP. ParM polymerized in ATP rapidly polymerizes to a maxima, and then gradually falls apart over time, with a decay constant proportional to the amount of ATP included in the reaction (15). In the presence of the non-hydrolyzable ATP analog, ATP- $\gamma$ -S, the polymerization signal remains at a plateau. These results suggest that the hydrolysis state of ParM can affect the stability of the polymer.

The nucleotide-dependent dynamics of ParM are critical to the *in vivo* function of the R1 spindle. Mutations of the Mg<sup>2+</sup> coordinating residue D170 completely eliminate all plasmid stabilization (12). This mutant also exhibits trans dominance, as small amounts of this mutant can abrogate plasmid partitioning in a wild type background. *In vivo* visualization of these mutants demonstrates that, in contrast to the 30% of cells that contained curly filaments, elimination of ATP hydrolysis yields 100% of the cells with long and linear filaments (18).

The nature of the interaction between the ParR/*parC* complex and ParM filaments has also been explored. As noted previously, ParM and ATP can increase the efficiency of pairing *parC* containing DNA by 2 fold (9). ParM has been shown to interact with ParR

by yeast 2-hybrid assays, and the ATPase activity of ParM was shown to be stimulated 6 fold by the addition of ParR and *parC* (12). It must be noted that the concentration of ParM used in this ATPase assay (56nM) is far beneath the lower bound ATP critical concentration of 1.5uM reported below (18). Surface Plasmon Resonance experiments indicated that *parC* bound to ParR, and that ATP-ParM filaments could then interact with this complex. This interaction could only be seen when ParM was added at or above 2.5uM and not at 1.5uM (19). Moller-Jensen et al (18) demonstrated that the addition of 20nM ParR and 2nM *parC* could induce the polymerization of 1uM ParM, a concentration at which ParM would not normally polymerize.

The gestalt of the above ~20 years of work has shown that the *par* operon is both necessary and sufficient to form force generating bipolar mitotic spindles. This statement carries heavy implication, as “sufficiency” implies that the *par* operon not only contains all of the structural components, but that it also 1) encodes mechanisms to spatially regulate the assembly of the spindle and 2) encodes an energetic mechanism to allow for spindle elongation.

In 2003 Moller-Jensen proposed a model for R1 plasmid segregation, where the replication of *parC* containing plasmids leads to their pairing by ParR and ParM (19). This pairing would then form a nucleation complex that nucleates ParM filaments. The ParM filaments would then elongate by addition of monomers at the ParR/ParM interface, while the free, unbound ends of the filaments would disassemble. This would lead to polymer treadmilling, with insertional polymerization at one end of the filaments and



disassembly at the other. They suggested that this would push the plasmids to either end of the cell in a manner similar to actin-mediated *Listeria* motility. While being an attractive hypothesis, this model does not take into account many features of their previous data. In fact, careful reexamination of the sum of past work lends a great deal of insight into how this system might function.

First, the ParM polymers appear to display a critical concentration beneath that of the cellular concentration. Polymerization of ParM in isolation was witnessed at 5 $\mu$ M but not at 1 $\mu$ M (18). These results suggest that the ParM steady state critical concentration was between 2.5-1.5 $\mu$ M. This value is much lower than the measured concentration of ParM monomers in the cell (15 $\mu$ M) (18), which indicates that ParM filaments will be present within the cell at steady state.

Second, the rapid spontaneous nucleation of ParM filaments should overshadow any ParR/*parC* mediated nucleation of filaments, as the rate of nucleation appears sufficiently fast as to not be limiting. This indicates that the nucleation of ParM should occur throughout the cell, as the concentration is much higher than the critical concentration. Rather, the presence of a critical concentration between 2.5-1.5 $\mu$ M, and the fact that the ParR/*parC* complex can facilitate polymerization beneath this value suggests that the ParR/*parC* complex can somehow decrease the critical concentration for ParM filament assembly.

Third, ADP-ParM appears to be less stable than ATP-ParM. While this was noted in the afore mentioned work (18), the magnitude of this difference in respect to eukaryotic actin is quite large, as ADP ParM polymers appear to depolymerize rapidly. Within eukaryotic actin, the difference between the ATP barbed end and ADP pointed end is only 10 fold. This subtle difference in affinities leads to treadmilling behavior, limited by the dissociation rate of ADP monomers from the pointed end. These observations beg the question whether, like eukaryotic actins, ParM also displays treadmilling behavior, or a more dramatic behavior such as dynamic instability.

The outstanding question of the *par* system is to understand, in a mechanistic and kinetic manner, how these three components can work together to form a force generating spindle. As previously noted, all of the genetic and evolutionary data suggests that this system is a fully self contained, exogenous segregation machine encoding all of the necessary components, regulation, and information needed to segregate the plasmids. As this system only contains a single polymer (ParM) and a single accessory factor/cargo (ParR/*parC*), this system provides an appealing system to work on within the time frame of a PhD thesis.

In order to fully elucidate how the *par* system functions, I have attempted to break the problem into two different regimes. First, I elucidated the kinetics of ParM filaments assembly to understand how the polymer behaves in isolation. This topic is the basis of Chapter 3, which is a reprint of my first publication. Following this, I sought to determine how the ParR/*parC* complex affects the kinetics and behavior of ParM

filaments, and whether (as assumed) these three components are sufficient *in vitro* to form a force generating spindle. This topic will be discussed in Chapter 4, a reprint of my second publication. As I have generated a great deal of other data that has not made its way into any publications, Chapter 5 will cover all of these other experiments, experimental conditions, and results for the sake of those who take up this system after me.

1. P. Zund, G. Lebek, *Plasmid* **3**, 65 (1980).
2. D. Godwin, J. Slater, *J Gen Microbiol* **111**, 201 (1979).
3. K. Gerdes, J. Møller-Jensen, R. Bugge Jensen, *Molecular microbiology* **37**, 455 (Aug, 2000).
4. R. Nakaya, A. Nakamura, Y. Murata, *Biochemical and biophysical research communications* **3**, 654 (Dec, 1960).
5. K. Gerdes, S. Molin, *J Mol Biol* **190**, 269 (1986).
6. M. Dam, K. Gerdes, *J Mol Biol* **236**, 1289 (1994).
7. C. Hoischen, A. Bolshoy, K. Gerdes, S. Diekmann, *Nucleic acids research* **32**, 5907 (Nov, 2004).
8. J. Moller-Jensen *et al.*, *Mol Cell* **12**, 1477 (2003).
9. R. Jensen, R. Lurz, K. Gerdes, *Proc Natl Acad Sci U S A* **95**, 8550 (1998).
10. R. Jensen, M. Dam, K. Gerdes, *J Mol Biol* **236**, 1299 (1994).
11. A. Breuner, R. Jensen, M. Dam, S. Pedersen, K. Gerdes, *Mol Microbiol* **20**, 581 (1996).
12. R. Jensen, K. Gerdes, *J Mol Biol* **269**, 505 (1997).

13. K. Bennett *et al.*, *Protein science: a publication of the Protein Society* **9**, 1503 (Sep, 2000).
14. R. Jensen, K. Gerdes, *Embo J* **18**, 4076 (1999).
15. J. Møller-Jensen, R. Jensen, J. Lowe, K. Gerdes, *Embo J* **21**, 3119 (2002).
16. P. Bork, C. Sander, A. Valencia, *Proceedings of the National Academy of Sciences of the United States of America* **89**, 7290 (Aug, 1992).
17. F. van den Ent, J. Møller-Jensen, L. Amos, K. Gerdes, J. Lowe, *Embo J* **21**, 6935 (2002).
18. J. Møller-Jensen, R. Jensen, J. Löwe, K. Gerdes, *The EMBO journal* **21**, 3119 (Jun, 2002).
19. J. Møller-Jensen *et al.*, *Molecular cell* **12**, 1477 (Dec, 2003).

## **Chapter 3**

### **Dynamic Instability in a DNA-segregating Prokaryotic Actin Homologue**

**Ethan C. Garner\*, Christopher S. Campbell\*, and R. Dyche Mullins**

**\* These authors contributed equally to this work**

**Published: Nov 5, 2004, Science, 306(5698):1021-5.**

## **Abstract**

Dynamic instability, the switching of a two-state polymer between phases of steady elongation and rapid shortening, is essential to the cellular function of microtubules, especially during chromosome segregation. Since the discovery of dynamic instability twenty years ago, no other biological polymer has been found to exhibit this behavior. We report here that the prokaryotic actin homolog ParM, whose assembly is required for segregation of large, low-copy plasmids, displays both dynamic instability and symmetrical, bi-directional polymerization. Dynamic instability of ParM is regulated by ATP hydrolysis and filaments are stabilized by a cap of ATP-bound monomers. ParM is not related to tubulin so its dynamic instability must have arisen by convergent evolution driven by a set of common constraints on polymer-based segregation of DNA.

## Results and Discussion

Recent work suggests that proteins related to eukaryotic actins (1-3) may be involved in prokaryotic chromosome segregation. Another example of prokaryotic DNA segregation, one that has been characterized in molecular detail, is the partitioning of R1 and R100 drug-resistance plasmids. These 100kb plasmids are found in many enteric pathogens and encode genes that confer antibiotic and heavy metal resistance as well as genes required for plasmid retention and conjugative transfer. They are stably maintained at 2-4 copies per cell (4) and have evolved an efficient mechanism to ensure inheritance by both daughters during cell division. The R1 *par* operon appears to construct a minimalist mitotic spindle from three components – *parC*, ParR, and ParM (5-7) – that positions pairs of plasmids at opposite ends of a rod-shaped bacterium (8). *parC* is a stretch of centromeric DNA that includes the R1 *par* promoter sequence (9); *parR* encodes a repressor protein that binds to the *parC* locus (9); and *parM* encodes an actin homolog. Purified ParM polymerizes in an ATP-dependent manner (7) into two-stranded helical filaments similar to conventional actin filaments (10) and binds specifically to the ParR/*parC* complex (8). *In vivo*, ParM filaments form a bundle that extends the length of the bacterium with plasmid DNA localized at each end, and polymerization of ParM has been postulated to provide force to push plasmids to opposite poles of the cell (7, 8). Because the system contains only three components we hypothesized that intrinsic assembly dynamics of ParM are critical to its role in segregating DNA.

We first investigated the kinetic polarity of ParM filament assembly by performing dual-color fluorescence microscopy on ParM filaments assembled *in vitro*. Both actin filaments and microtubules are structurally and kinetically polarized so that one end of

the polymer elongates faster than the other and ultrastructural studies indicate that ParM filaments have a structural polarity similar to that of actin filaments (10). We polymerized filaments labeled with Alexa-488 (green) by adding the non-hydrolyzable ATP analog AMPPNP, and then added Cy3-labeled (red) ParM. Most filaments observed (91%) had green centers with equal amounts of red fluorescence on each end (Fig. 1A), suggesting that, unlike previously characterized nucleotide-dependent polymers, ParM filament polymerization is kinetically symmetrical.

We next examined polymerization dynamics of individual ParM filaments using total internal reflection fluorescence (TIRF) microscopy of Alexa-488-labeled ParM. In the presence of AMPPNP, ParM filaments are very long (Fig. 1B, left) and grow symmetrically with equal rates of assembly at each end (Fig. 1C and Movies S1-S2). Electron microscopy of polymeric ParM reveals well-separated, individual filaments with no obvious bundles (7, 10). This observation, along with the fact that we observe approximately uniform fluorescence along the length of labeled ParM filaments, argues that we are observing individual filaments and not anti-parallel bundles of asymmetrically-elongating filaments. In the presence of hydrolysable ATP, ParM filaments also elongate symmetrically but are much shorter (Fig. 1B, right) and more dynamic (Movies S3-S5). After growing for a variable length of time, ATP-ParM filaments abruptly switch from bi-directional elongation to rapid, endwise disassembly (Fig. 1D). In most cases disassembly is unidirectional and in all cases observed ( $n > 530$ ), the switch from elongation to shortening results in complete disassembly of the filament. Shortening does not reflect detachment of the filament from the coverslip, as detachment results in disappearance of the filament in a single step (see supporting online text). At all



ParM concentrations above  $2\mu\text{M}$  the average filament length is 1.5 microns, suggesting that length is determined primarily by an intrinsic property of the filaments (Fig. 1F). ATP-ParM filaments elongate with a rate constant of  $5.3 \pm 1.3 \mu\text{M}^{-1}\text{sec}^{-1}$  ( $n=50$ ) at each end, similar to that of the fast-growing, barbed end of actin filaments. After switching from growth to shortening, filaments disassemble at a rate of  $64 \pm 20 \text{ sec}^{-1}$  ( $n=16$ ) (Fig. 1E). The time spent growing and the maximum length achieved before catastrophic disassembly are variable, suggesting that the switch from elongation to shortening is stochastic. This property of switching between phases of elongation and rapid shortening is called dynamic instability, and has, until now, been observed only in eukaryotic microtubules.

ParM filaments, like microtubules and conventional actin filaments, assemble via a nucleation-condensation mechanism, characterized by: (i) the existence of a critical concentration, above which polymer forms and below which it does not, and (ii) a concentration-dependent time lag in spontaneous polymerization, during which stable nuclei assemble. We used fluorescence resonance energy transfer (FRET) to monitor ParM polymerization kinetics at varying concentrations of protein and ATP (see supporting online text for assay conditions and control experiments). Using both FRET and high-speed pelleting assays we determined an apparent steady-state critical concentration of  $2.3 \mu\text{M}$  for  $\text{Mg}^{2+}$ -ATP ParM (Fig. 3B and S3A). This value is consistent with estimates based on fluorescence microscopy (Fig. 1F). In addition, ATP-induced polymerization of ParM filaments proceeds after a time lag that decreases with increasing protein concentration (Fig. 2A inset and S3B).

We define the filament nucleus as the smallest oligomer more likely to elongate than to fall apart. Using this definition, the maximum rate of polymer assembly is approximately  $k_{e+}k_{n+}[m^*]^n$ , where  $[m^*]$  is the initial monomer concentration minus the critical concentration,  $k_{e+}$  is the rate constant for polymer elongation,  $k_{n+}$  is the rate constant for the nucleation reaction, and  $n$  is the number of monomers required to form a nucleus (11). By plotting the logarithm of the maximum rate of polymerization versus the logarithm of the protein concentration (11, 12) we determined that conventional actin and ParM both elongate from a nucleus composed of three monomers (Fig. 2A) – as expected for a two-stranded, helical polymer (13). Although the slopes are identical, the ParM polymerization data are shifted upward by about 2.5 log units compared to the data for conventional actin. This indicates that the product of the nucleation and elongation rates is 300-fold higher for ParM than for actin. Because the elongation rates are approximately equal, the shift in the ParM data must reflect a 300-fold faster rate of spontaneous nucleation compared to conventional actin.

Consistent with previous studies (7), we find that the half-life of ParM in solution increases linearly with increasing concentration of ATP, suggesting that polymer stability is regulated by ATP hydrolysis (Fig. 2B). We note that bulk assembly kinetics of ParM are triphasic, with an initial peak in polymer concentration followed by a dip and then a slow approach to equilibrium (see supporting online text for further discussion of polymerization kinetics). The initial rise and fall in ParM polymer appears to represent a population of rapidly-nucleated filaments that elongate in synchrony and undergo somewhat synchronous catastrophe. Microtubules exhibit similar synchronous behavior under conditions where nucleation is fast and/or nucleotide dissociation is slow (14, 15).

Consistent with the notion that ATP hydrolysis regulates ParM filament stability, we find that ADP-ParM filaments are extremely unstable, with a critical concentration of approximately  $100\mu\text{M}$  (16). To determine whether hydrolysis of ATP itself or dissociation of cleaved phosphate destabilizes the filament we tested the effect of the phosphate analog, beryllium fluoride ( $\text{BeF}_3$ ) on ParM filament stability.  $\text{BeF}_3$  has been used to stabilize ADP actin filaments (17) and it appears to induce a conformation similar to that of filaments after cleavage of the  $\gamma$ -phosphate of the bound ATP but before phosphate dissociation ( $\text{ADP-P}_i$ ). Addition of  $\text{BeF}_3$  and ADP does not induce assembly of ParM filaments but  $\text{BeF}_3$  does stabilize filaments formed in low concentrations of ATP (Fig. 2C). By TIRF microscopy, the length distribution of  $\text{BeF}_3$ -ParM filaments is identical to that of ATP-ParM filaments (Fig. S1A) but  $\text{BeF}_3$ -ParM filaments do not exhibit dynamic instability (Movie S6). By FRET and high-speed pelleting assays, the critical concentration of  $\text{BeF}_3$ -ParM is  $0.6\ \mu\text{M}$  (Fig. 3B). It appears that the steady-state monomer concentration that we measure for ATP ParM ( $2.3\ \mu\text{M}$ ) is the sum of the critical concentrations of the ATP- and ADP-filament ends weighted by their relative abundance.

Polymerization of ParM stimulates hydrolysis of bound ATP (7), so we directly compared the kinetics of ParM polymerization and ATP hydrolysis in side-by-side assays. To measure polymerization, we mixed labeled ParM ( $15\mu\text{M}$ ) with  $200\mu\text{M}$  ATP in a rapid mixer and recorded the FRET signal (Fig. 2D). To measure hydrolysis, we mixed material from the same sample with  $200\mu\text{M}$  ATP doped with  $\gamma$ - $^{32}\text{P}$ ATP in a quenched-flow rapid mixing device. Hydrolysis follows filament assembly and the instantaneous rate of hydrolysis is proportional to the measured polymer concentration (Fig. 2D inset).

The hydrolysis stimulated by polymerization is rapid, with a rate constant of  $0.2 \text{ sec}^{-1}$ . This is similar to the rates of hydrolysis in actin filaments ( $0.3 \text{ sec}^{-1}$ ) (18) and in polymers of the bacterial tubulin homolog *ftsZ* ( $0.13 \text{ sec}^{-1}$ ) (19) and is fast enough to account for the observed rapid dynamics of ParM filaments. Complete loss of ParM polymer does not correlate with complete exhaustion of ATP in the reaction, suggesting that low concentrations of ADP generated in the reaction inhibit polymerization of ParM. Further work suggested that free ADP affects ParM filament stability (see supporting online text). All of our observations of intrinsic dynamic instability were made under conditions where this additional ADP-dependent destabilizing effect is not observed.

To determine conclusively whether nucleotide hydrolysis drives dynamic instability of ParM filaments, we mutated residues required for ATP hydrolysis by ParM and tested the effect on filament stability. Based on the model of Vorobiev *et. al.* for ATP hydrolysis by actin (20), we mutated glutamate 148 of ParM to alanine (Fig. S4A) and tested the effect on polymerization and ATP hydrolysis (see Supplementary Material). This mutation (E148A) abolishes all detectable ATPase activity, even at high protein concentrations (Fig. 3A inset). Like wild-type ParM, the E148A mutant assembles into filaments in a symmetrical bi-directional manner (Movie S7), however, unlike wild-type ParM, E148A filaments are stable in low ATP concentrations (Fig. 3A). TIRF microscopy reveals that E148A-ParM filaments are long and stable in the presence of ATP, similar to wild-type ParM filaments formed in the presence of AMPPNP (Fig. S4B). Nucleation of E148A-ParM filaments is slower than that of wild-type filaments but, once formed, mutant filaments elongate at the same rate as wild-type (Fig. S4D). Finally, the critical

concentration of the E148A mutant (0.68  $\mu\text{M}$ ) is close to that of  $\text{BeF}_3$ -bound wild-type ParM (0.6  $\mu\text{M}$ ) (Fig. 3B).

A basic assumption of nucleotide-dependent dynamic instability is that the polymer is stable as long as the ends retain a cap of nucleotide triphosphate-bound monomers (21, 22). Once this cap is lost, the polymer rapidly depolymerizes. To determine whether ParM filaments are stabilized by an ATP cap, we mixed wild-type and E148A ParM in different ratios to determine whether substoichiometric amounts of E148A can stabilize wild-type ParM filaments. In pelleting experiments small amounts of E148A decrease the critical concentration of wildtype ParM (Fig. 3C). Above 20% E148A, the total amount of ParM in the supernatant fraction remains constant and is close to the measured critical concentration of the E148A mutant and wild-type  $\text{BeF}_3$ -ParM. This result suggests that subsaturating amounts of ATP-bound ParM can stabilize wild-type polymer, consistent with the ability of an ATP cap to stabilize ADP-bound filaments.

TIRF microscopy assays also demonstrate that small amounts of E148A ParM have significant effects on filament stability. Filaments doped with 20% E148A are very stable (Fig S4C) and elongate in a bipolar fashion, similar to filaments composed entirely of E148A (Movie S8). Samples with 10% E148A contain a subset of filaments that remain stable for long periods of time. At 3% and 5% E148A fewer filaments are stable and samples doped with 1% E148A are identical to wild-type ParM. At dopings of 3% and 5%, we observe filaments that experience periods of elongation and rapid shortening but do not undergo complete disassembly (Fig. 3D). This behavior is similar to the phenomenon of ‘rescue’ observed in dynamic instability of microtubules.

We note three important differences between the kinetics of ParM filament assembly and those of conventional actin. First, ADP-ParM monomers dissociate from filament ends approximately 100-times faster than ADP-actin monomers (Table 1). ADP-actin filaments require severing factors such as cofilin to promote complete disassembly (23) whereas the fast off-rate of ADP-ParM monomers from the end of the filament produces a microtubule-like dynamic instability (Fig. 4A). Second, the nucleation rate of ParM filaments is 300 times faster than that of actin filaments. Evolution has erected a large kinetic barrier to spontaneous nucleation of eukaryotic actins so that actin requires nucleation factors such as the Arp2/3 complex (24) and formins (25) to form filaments *in vivo*. The rate of the spontaneous ParM filament formation is similar to that of conventional actin in the presence of formins (26). Third, the rate of ADP dissociation from ParM monomers is 100-fold faster than from actin, which requires profilin to achieve the same rate of nucleotide dissociation and exchange (23). Thus, ParM appears to be kinetically tuned to operate independently of exogenous nucleation, depolymerization, and nucleotide exchange factors.

Both ParM filaments and microtubules segregate DNA and both exhibit dynamic instability. Dynamic instability of tubulin is driven by GTP hydrolysis and, during mitosis, dynamic instability enables the ends of microtubules to search intracellular space efficiently and to locate kinetochores of unattached chromosomes (for a review, see (27)). Dynamic instability of ParM filaments is driven by ATP hydrolysis and mutations in ParM that perturb nucleotide hydrolysis abolish plasmid partitioning (28, 29), suggesting that ParM dynamic instability is required for plasmid segregation. We hypothesize that ParM dynamic instability enables filament ends to efficiently locate and capture plasmid

DNA targets. The average length of ATP-ParM filaments (1.5  $\mu\text{m}$ ) is comparable to the length of many rod-shaped bacteria, so ParM filaments may be kinetically tuned to search the volume of a bacterial cell and capture ParR/*parC* complexes. In addition, bi-directional assembly would promote segregation without requiring anti-parallel filaments to slide past each other.

Moller-Jensen et al. (7) reported that the ParR/*parC* complex nucleates ParM polymerization. Their data, however, show only that ParR/*parC* can stabilize ParM filaments below the steady-state ATP critical concentration. Given the low nucleation barrier and high cellular concentrations of ParM (12-14  $\mu\text{M}$ ) (7), nucleation is unlikely to be the point at which ParM assembly is regulated. It appears that the property of ParM kinetics most amenable to regulation is filament stability. We propose that, at cellular concentrations of ParM, spontaneous nucleation and filament elongation occur throughout the cell and that, unless stabilized by interaction with ParR/*parC* (8), these filaments will spontaneously disassemble. In this model, only filaments with plasmid bound to both ends are stabilized against catastrophic disassembly (8) (7); and bi-directional elongation of ParM filaments at the interface with the ParR/*parC* complex drives plasmid segregation (Fig 4B). Such insertional polymerization mechanisms have been proposed for elongating microtubule ends attached to kinetochores and actin filaments bound to formin-family proteins.

## References

1. T. Kruse, J. Moller-Jensen, A. Lobner-Olesen, K. Gerdes, *Embo J* **22**, 5283 (Oct 1, 2003).
2. H. J. Soufo, P. L. Graumann, *Curr Biol* **13**, 1916 (Oct 28, 2003).
3. Z. Gitai, N. Dye, L. Shapiro, *Proc Natl Acad Sci U S A* (May 24, 2004).
4. K. Nordstrom, L. C. Ingram, A. Lundback, *J Bacteriol* **110**, 562 (May, 1972).
5. K. Gerdes, S. Molin, *J Mol Biol* **190**, 269 (Aug 5, 1986).
6. K. Gerdes, J. E. Larsen, S. Molin, *J Bacteriol* **161**, 292 (Jan, 1985).
7. J. Moller-Jensen, R. B. Jensen, J. Lowe, K. Gerdes, *Embo J* **21**, 3119 (Jun 17, 2002).
8. J. Moller-Jensen *et al.*, *Mol Cell* **12**, 1477 (Dec, 2003).
9. M. Dam, K. Gerdes, *J Mol Biol* **236**, 1289 (Mar 11, 1994).
10. F. van den Ent, J. Moller-Jensen, L. A. Amos, K. Gerdes, J. Lowe, *Embo J* **21**, 6935 (Dec 16, 2002).
11. H. Wendel, P. Dancker, *Biochim Biophys Acta* **915**, 199 (Sep 24, 1987).
12. E. Nishida, H. Sakai, *J Biochem (Tokyo)* **93**, 1011 (Apr, 1983).
13. F. Oosawa, M. Kasai, *J Mol Biol* **4**, 10 (Jan, 1962).
14. E. M. Mandelkow, G. Lange, A. Jagla, U. Spann, E. Mandelkow, *Embo J* **7**, 357 (Feb, 1988).
15. M. F. Carlier, R. Melki, D. Pantaloni, T. L. Hill, Y. Chen, *Proc Natl Acad Sci U S A* **84**, 5257 (Aug, 1987).
16. Data not shown.
17. C. Combeau, M. F. Carlier, *J Biol Chem* **263**, 17429 (Nov 25, 1988).



18. L. Blanchoin, T. D. Pollard, *Biochemistry* **41**, 597 (Jan 15, 2002).
19. L. Romberg, T. J. Mitchison, *Biochemistry* **43**, 282 (Jan 13, 2004).
20. S. Vorobiev *et al.*, *Proc Natl Acad Sci U S A* **100**, 5760 (May 13, 2003).
21. D. Panda, H. P. Miller, L. Wilson, *Biochemistry* **41**, 1609 (Feb 5, 2002).
22. D. N. Drechsel, M. W. Kirschner, *Curr Biol* **4**, 1053 (Dec 1, 1994).
23. V. K. Vinson, E. M. De La Cruz, H. N. Higgs, T. D. Pollard, *Biochemistry* **37**, 10871 (Aug 4, 1998).
24. M. D. Welch, R. D. Mullins, *Annu Rev Cell Dev Biol* **18**, 247 (2002).
25. S. H. Zigmond, *Curr Opin Cell Biol* **16**, 99 (Feb, 2004).
26. M. Pring, M. Evangelista, C. Boone, C. Yang, S. H. Zigmond, *Biochemistry* **42**, 486 (Jan 21, 2003).
27. T. J. Mitchison, E. D. Salmon, *Nat Cell Biol* **3**, E17 (Jan, 2001).
28. R. B. Jensen, K. Gerdes, *J Mol Biol* **269**, 505 (Jun 20, 1997).
29. R. B. Jensen, K. Gerdes, *Embo J* **18**, 4076 (Jul 15, 1999).
30. Supporting Online Material  
[www.sciencemag.org](http://www.sciencemag.org)  
Materials and Methods  
Supporting Online Text  
Figs. S1, S2, S3, S4  
Movie S1, S2, S3, S4, S5, S6, S7, S8, S9
31. We are grateful to members of the Mullins lab for moral support, and helpful discussions. We thank Laura Frost for giving us the R100 plasmid, Nico Stuurman and Adam Douglas for their invaluable assistance with TIRF

microscopy, and Michio Tanegawa for advice on FRET. We thank Tim Mitchison, Kathleen Ryan, Ron Vale, Mark Dayel, and Quincey Justman for critical readings of the manuscript. This work was supported by grants to RDM from the National Institutes of Health (GM61010-01), the Pew Charitable Trust (P0325SC), and the Sandler Family Supporting Foundation. Both ECG and CSC are supported by National Science Foundation Pre-doctoral Fellowships. CSC acknowledges Jimmy for continuing support and advice and ECG acknowledges BZA for being triumphant.

Figure 1

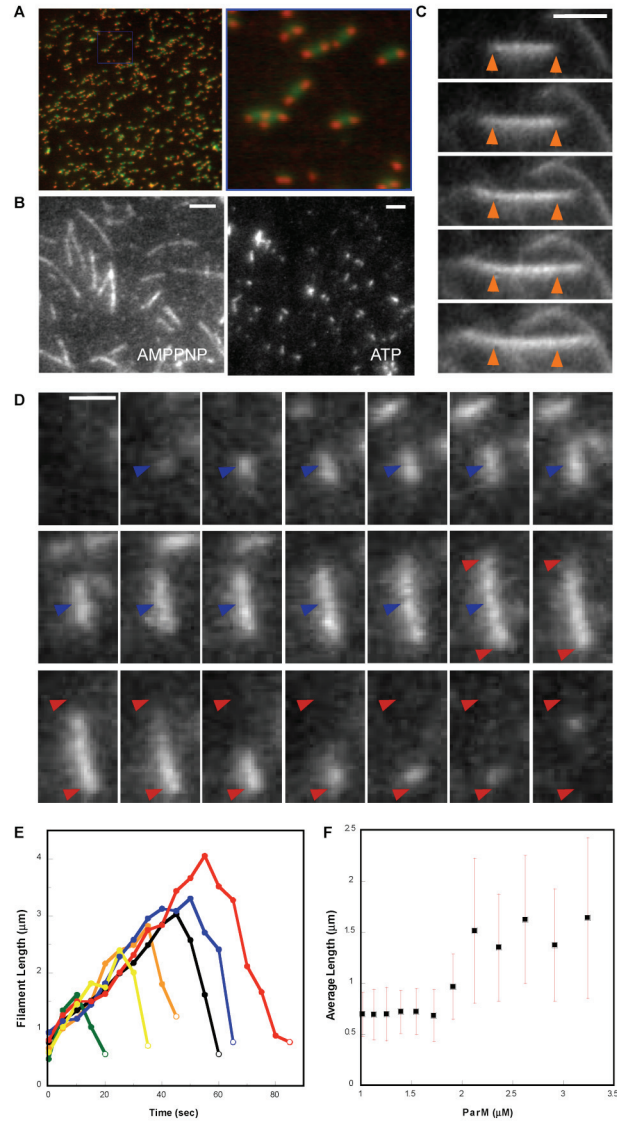


Figure 2

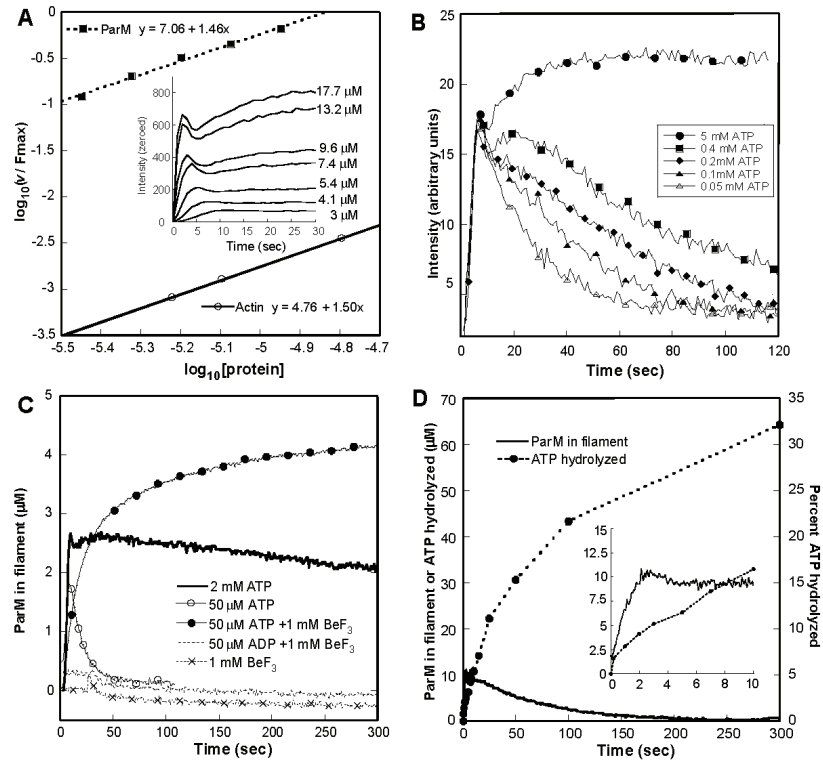


Figure 3

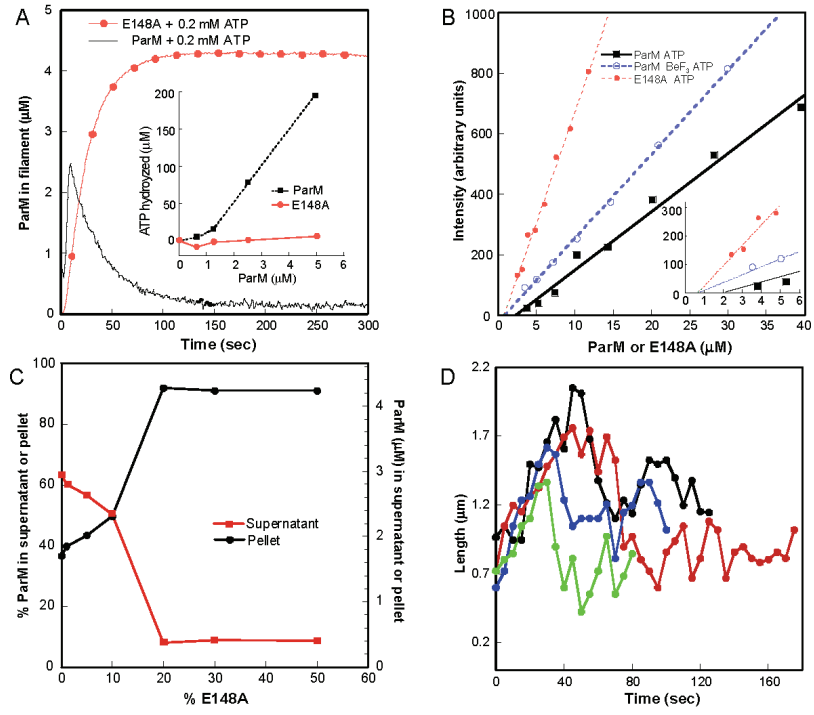
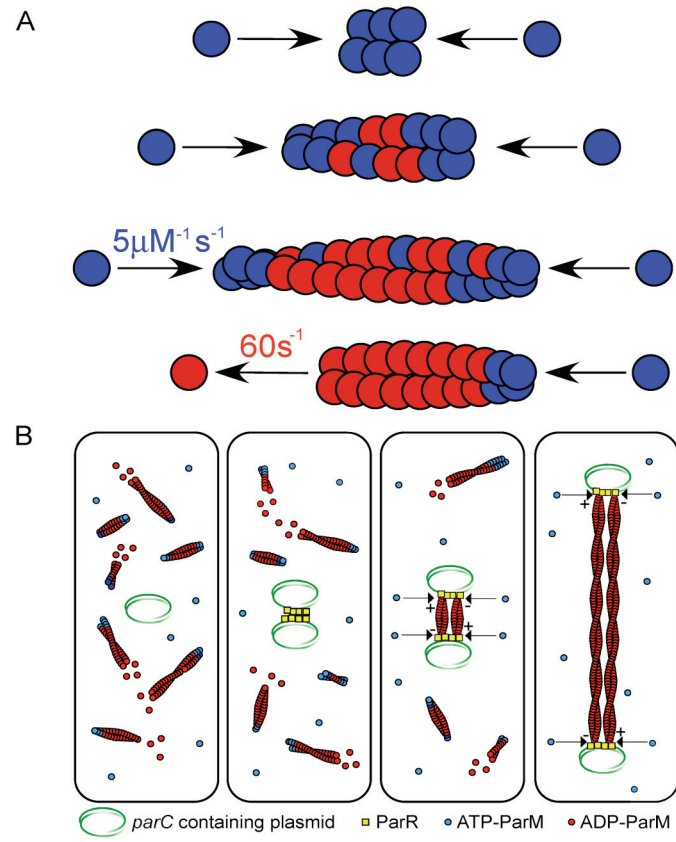


Figure 4



## Figure legends

### Figure 1. Direct observation of bipolar elongation and dynamic instability.

- (A) ParM filaments elongate bi-directionally. 1 $\mu$ L of 4.3 $\mu$ M ParM labeled with Alexa-488 (green) was induced to polymerize on poly-L-lysine-coated coverslips by the addition of 0.2 $\mu$ L of 100mM AMPPNP. After 30 seconds, we added 1 $\mu$ L of 3.1 $\mu$ M monomeric ParM labeled with Cy3 (red). After 1 minute, the reaction was diluted with 20 $\mu$ L of Buffer F and visualized by fluorescence microscopy.
- (B) Hydrolysis of ATP affects ParM filament length. Total Internal Reflection (TIRF) microscopy of 2.7 $\mu$ M Alexa-488-labeled ParM polymerized by addition of 10mM of either the non-hydrolyzable ATP analog AMPPNP (left) or ATP (right). Scale bars are 5 microns.
- (C) AMPPNP ParM filaments elongate at equal rates from both ends. Time-lapse TIRF microscopy of 2.7 $\mu$ M 10% Alexa-488-labeled ParM polymerized by addition of 10mM AMPPNP. Orange arrows indicate the initial positions of the filament ends. Images are 50 seconds apart and the scale bar is 5 microns.
- (D) In the presence of hydrolysable ATP, ParM filaments polymerize with no detectable kinetic polarity and exhibit dynamic instability. Time-lapse TIRF of 2.7 $\mu$ M 10% Alexa-488-labeled ParM polymerized by addition of 10mM ATP. The blue arrow designates the starting point of the filament and the red arrows show the endpoints prior to depolymerization. Images were collected 5 seconds apart. Scale bar is 2 microns.
- (E) The rates of ParM filament elongation and shortening are relatively constant from filament to filament, while the time spent in the elongation phase is variable.

Length of filaments versus time for 6 representative filaments polymerized in ATP. After switching from growth to shortening, every filament we observed disappeared completely. An open circle denotes that the given filament disappeared in the next frame.

- (F) ParM filaments appear above 2  $\mu\text{M}$  and have a concentration independent average length of 1.5 microns. Below 2 $\mu\text{M}$ , most fluorescent structures observed are the size of diffraction-limited spots (0.75 microns) and probably do not represent bona fide filaments.

**Figure 2. Kinetics of ParM polymerization measured by fluorescence resonance energy transfer (FRET).**

- (A) Determination of the nucleus size and relative nucleation rates of ParM and conventional actin filaments. FRET-labeled ParM (unlabeled ParM doped with 15% Cy3- and 15% Cy5-labeled monomer) was polymerized at varying concentrations by the addition of 5mM ATP (inset). The maximal velocity of the polymerization signal was divided by the maximal fluorescence and the log of this value plotted against the log of the concentration of protein. The lines in the graph have a slope proportional to nucleus size ( $n-1$ ) and the x-intercept is the relative nucleation rate ( $k_n^+$ ). This analysis demonstrates that ParM and actin both elongate from nuclei composed of three monomers and that spontaneous nucleation of ParM filaments is 300-fold faster than that of actin.
- (B) The lifetime of ParM filaments depends on ATP concentration. We combined 5 $\mu\text{M}$  FRET-labeled ParM with the indicated amount of ATP using a rapid mixer and monitored polymer content by FRET signal.



- (C) The phosphate analog  $\text{BeF}_3$  stabilizes ParM filaments. We mixed  $5\mu\text{M}$  FRET-labeled ParM with ADP or ATP in the presence or absence of  $1\text{mM}$   $\text{BeF}_3$  using a rapid mixer and monitored polymer content by FRET.
- (D) ATP hydrolysis lags behind ParM polymerization. To monitor polymerization and ATP hydrolysis we mixed  $15\mu\text{M}$  FRET-labeled ParM with  $200\mu\text{M}$  ATP doped with  $\gamma[^{32}\text{P}]$ -labeled ATP. We monitored polymerization by mixing in a stopped-flow rapid mixer and monitoring FRET. We monitored ATP hydrolysis by mixing the samples in a quenched-flow rapid mixer and measuring the amount of radioactive phosphate released at various time points. Total polymer and cleaved phosphate are plotted on the same scale. Inset. Expansion of the first 10 seconds of the plot.

**Figure 3. Small amounts of non-hydrolyzing mutant ParM stabilize wild-type ParM filaments**

- (A) Mutating glutamic acid 148 of ParM to alanine (E148A) abolishes hydrolysis of ATP and stabilizes ParM filaments. We measured polymerization kinetics by FRET using  $5\mu\text{M}$  FRET-labeled E148A or wild-type ParM. We induced polymerization with  $200\mu\text{M}$  ATP using a stopped-flow rapid mixer. Inset. Bulk measurements of ATP hydrolysis by wild-type and E148A ParM.  $5\mu\text{M}$  wild-type or E148A ParM at the indicated concentrations were combined with  $1\text{mM}$  ATP doped with ATP- $\gamma$ - $^{32}\text{P}$ . The amount of cleaved radioactive phosphate was determined after 15 minutes.

**(B)** The critical concentrations of the ATP (ATP + E148A) and ADP-Pi (ATP + BeF<sub>3</sub> + ParM) states are 4 fold lower than the apparent ATP-ParM critical concentration. 95µL of serially diluted FRET labeled wild-type ParM or E148A was combined with 5mM ATP or 5mM ATP plus 1mM BeF<sub>3</sub> within a cuvette. The unpolymerized signal was subtracted from the polymerized signal and plotted against the concentration of protein. The x-intercept values are taken as the critical concentrations.

**(C)** Substoichiometric amounts of the hydrolysis-deficient ParM mutant stabilize ParM filaments. 5.1µM Cy3 labeled ParM was combined with 5.1 µM Cy5 labeled E148A in the indicated ratios, polymerized with 10mM ATP, and spun in an ultracentrifuge. Samples of supernatant and pellet were run on an SDS-PAGE gel and quantitated using a fluorescent imager. Graph indicates the amounts of Cy3-ParM fluorescence. In the absence of E148A mutant ParM the critical concentration of ParM is 2.7 µM. Addition of low concentrations of E148A ParM decreases the critical concentration. At 20% doping of the mutant the critical concentration falls to approximately 0.5 µM – the critical concentration of E148A ParM alone.

**(D)** Substoichiometric concentrations of E148A ParM promote rescue of depolymerizing ParM filaments. We plotted filament length versus time for 4 individual filaments composed of 5% E148A and 95% wild-type ParM. Time zero corresponds to the initiation of a period of elongation. Unlike filaments composed entirely of wild-type ParM, the length of the composite filaments

oscillate and the switch from elongation to shortening does not always result in complete filament disassembly.

**Figure 4. Model for dynamic instability and *in vivo* function of ParM filaments.**

**(A)** Kinetic model for the dynamic instability of ParM. Once a nucleus is formed, the polymer elongates in a kinetically symmetrical manner. Polymerization induces ATP hydrolysis and ADP-bound monomers accumulate in the center of the filament. The filament remains stable as long as it maintains an ATP cap at both ends. When the cap at one end is lost, the polymer rapidly disassembles from that end.

**(B)** Model for ParM mediated plasmid segregation. ParM filaments spontaneously nucleate and elongate throughout the cell. Because of hydrolysis-induced dynamic instability these polymers are unstable and they rapidly disassemble. Upon plasmid replication, 2 ParR/*parC* complexes form and are competent to capture and stabilize both ends of a set of ParM filaments. Through a mechanism of insertional polymerization at the ParM/ParR interface (arrows), the spindle elongates bidirectionally, and pushes plasmids to the opposing ends of the cell.

**Table 1****Kinetic parameters of ParM and actin**(All values for Mg<sup>2+</sup> bound form unless otherwise indicated.)

	Actin	ParM	Determination
Steady-state ATP Critical Concentration (Mg <sup>2+</sup> )	100nM	2.3μM	Pelleting, FRET assay, Microscopy
Steady-state ATP Critical Concentration (Ca <sup>2+</sup> )	440nM (in 100mM KCl)	6.8μM	Pelleting
ATP Critical Concentration	barbed end - 100nM pointed end - 600nM	550-680nM	FRET assay (BeF-ATP-ParM and ATP-E148A)
ADP Critical Concentration	1μM	~100μM	Pelleting
ATP-Monomer On-Rate	barbed end - 10 (μM <sup>-1</sup> , s <sup>-1</sup> ) pointed end - 1 (μM <sup>-1</sup> , s <sup>-1</sup> )	4-5.3 (μM <sup>-1</sup> , s <sup>-1</sup> )	Microscopy (Wild-type and E148A)
ADP-Monomer Off-Rate	barbed end - NA pointed end - 0.2/s	64/s	Microscopy (Catastrophe rate of ATP-ParM)
ATP Kd	1.2nM	42nM k- 0.008 sec <sup>-1</sup> k+ 2.32X10 <sup>5</sup> M <sup>-1</sup> sec <sup>-1</sup>	ε-ATP fluorimetry
ADP Kd	0.3nM	2.4μM k- 0.56 sec <sup>-1</sup> k+ 1.85X10 <sup>5</sup> M <sup>-1</sup> sec <sup>-1</sup>	ε-ADP fluorimetry
Hydrolysis Rate (estimated)	0.3/s	0.1-0.2/s	Modeling
Nucleation rate	1x	300x	Concentration dependence of maximal velocity

## Supplementary Text

### **TIRF controls for filament detachment.**

To ensure that disappearance of ParM filaments was due to depolymerization rather than detachment of filaments from the coverslip, we compared the behavior of dynamic wild-type ParM filaments with BeF<sub>3</sub>-stabilized ParM filaments. These two samples have very similar length distributions (Fig S1A), ensuring that any differences in the rate of filament disappearance are not a result of differences in filament length.

We randomly selected individual filaments from individual frames of the time-lapse sequences and then followed them through the sequence until they disappeared. All randomly-selected, ATP-ParM filaments disappear completely within 120 seconds (Fig S1B). In contrast, filaments of the same length, stabilized with BeF<sub>3</sub> remain visible for more than 300 seconds. This indicates that the observed dynamics of ATP-ParM filaments are not due to coverslip detachment and diffusion out of the evanescent field. In addition, the majority of ATP-ParM filaments disappear by endwise shortening over multiple time-lapse images. BeF<sub>3</sub>-stabilized filaments, on the other hand, disappear in a single step from one image to the next.

### **FRET assay for ParM polymerization.**

Previous studies used light scattering to monitor ParM filament assembly (5). We wanted a more robust, fluorescence-based assay that is linear over a wider range of concentrations and filament lengths. For this purpose, we engineered a C-terminal cysteine into ParM that we could label using fluorescent dyes containing sulfhydryl-reactive functional groups. We first labeled this residue with environmentally-sensitive

dyes (including pyrene) and looked for a polymerization-induced change in fluorescence. This approach, however, did not yield a satisfactory polymerization-dependent signal. After some trial-and-error, we developed an assay based on fluorescence resonance energy transfer (FRET), in which polymerization induces energy transfer between adjacent dye-labeled monomers in the filament (a distance of 49 angstroms (*l*)). This approach has been used previously to monitor actin assembly kinetics (6). We doped purified, unlabeled ParM with 15% Cy3- and 15% Cy5-labeled monomers. To minimize the effect of donor emission and direct acceptor excitation on our FRET signal, we excited our samples at 514nm and measured emission at 690nm, wavelengths far from the Cy5 emission and Cy3 excitation maxima respectively.

We performed several control experiments to verify that the polymerization-induced increase in fluorescence was indeed caused by energy transfer. We measured emission spectra of 15  $\mu$ M FRET-labeled ParM in the absence and presence of ATP. Addition of ATP decreased fluorescence at 570 nm (Cy3 donor emission) and increased fluorescence between 650-700 nm (Cy5 acceptor emission), a hallmark of energy transfer (Fig. S2A). To determine the influence of scattered emission light on our FRET signal we inserted a long-pass filter (Schott glass KV550, Melles Griot) in series with the emission monochromator of our fluorimeter. We observed the same fluorescence changes in the absence and presence of the additional filter, indicating that light scattering does not contribute to our FRET signal. Addition of ATP to ParM doped only with Cy3- (Fig. S2B) or Cy5-labeled monomers (Fig. S2C) does not induce a fluorescence increase between 650-700 nm, but rather a decrease in total fluorescence in both cases. This effect is similar to the polymerization-induced self-quenching observed previously with

fluorescein-labeled actin (6). Correcting for self-quenching, we estimate that polymerization of 15  $\mu\text{M}$  ParM doped with 15% each of Cy3- and Cy5-labeled monomers results in transfer of 5% of the energy absorbed by the donor to the acceptor. This results in a 60% increase in fluorescence at the acceptor emission maximum.

We also performed time-domain control experiments on our FRET polymerization assay. Using excitation and emission wavelengths of 514 nm and 690 nm, we found that addition of ATP (but not ADP) produces a rapid increase in fluorescence that requires both Cy3- and Cy5-labeled proteins (Fig. S2D). Light scattering (at 310nm) and FRET measurements on the same sample yield nearly identical curves (Fig. S2E). Monitoring donor (Cy3) emission in the presence of both donor and acceptor yields a negative change in fluorescence with identical kinetics (7).

### **Polymerization kinetics of ParM using the FRET assay**

Consistent with previous studies (5), we find that ATP-induced assembly of ParM filaments requires a divalent cation ( $\text{Mg}^{2+}$  or  $\text{Ca}^{2+}$ ), as excess EDTA inhibits polymerization of  $\text{Mg}^{2+}$ -ATP-ParM. We also find that  $\text{Ca}^{2+}$ -ATP-ParM can polymerize, with a critical concentration of 6.8 $\mu\text{M}$  (7), in the absence of  $\text{Mg}^{2+}$ . We also note that ParM assembly kinetics are triphasic: Addition of ATP induces an initial, rapid increase in polymer content with kinetics that depend on the concentration of ParM (Fig. 2A inset) but that are relatively insensitive to the concentration of ATP (Fig. 2B). Although the initial rate of polymerization is rapid, fast kinetic experiments demonstrate that there is indeed a concentration dependent lag time of polymerization (Fig. S3B), as expected for a nucleation-condensation polymer. The rapid increase of initial polymerization is

followed by a highly-reproducible decrease in polymer content that we observe by both FRET and light scattering assays. This decrease is most obvious at high ParM concentrations and produces a characteristic ‘hump’ in the data (Fig. 2A inset, 2B, S3B) that is followed by a slower approach to equilibrium with kinetics that depend on ATP concentration (Fig. 2B). This hump is not seen with non-hydrolyzing ParM mutants; or when wild-type ParM is polymerized with nonhydrolyzable ATP analogs; or in the presence of  $\text{BeF}_3$ , consistent with the idea that the rapid decrease in signal reflects synchronous depolymerization due to dynamic instability. This behavior was not observed in previous studies (5) as the previous work collected data at 5 second intervals and mixed ParM with ATP by hand rather than using a rapid mixer. These techniques would not have provided sufficient mixing or time resolution to see the triphasic signal.

### **ADP destabilization of ParM Filaments**

We noted that, at low concentrations of ATP, depolymerization of ParM does not correlate with exhaustion of ATP in the reaction. One hundred seconds after addition of 200  $\mu\text{M}$  ATP to 15  $\mu\text{M}$  ParM, the polymerization signal returns almost to baseline. At this time point, however, only 20% of the ATP has been hydrolyzed (Fig. 2D). To verify that this was a ‘poisoning’ effect of the ADP generated during the reaction we tested the effect of ADP on spontaneous ParM assembly and found that polymerization is completely inhibited at a 1:4 molar ratio of ADP:ATP (7). This is consistent with previous work by Moller-Jensen et al. (5) that suggested low concentrations of ADP might inhibit polymerization of ParM. We considered two possible explanations for this effect: (i) ParM monomers might bind ADP with much higher affinity than ATP or (ii)



low concentrations of ADP in solution might somehow destabilize ParM filaments. To test the first possibility we measured the rate constants for association and dissociation of ATP and ADP with ParM monomers (Table 1). Monomeric ParM binds ATP 60-fold more tightly than ADP, ruling out the first possible explanation for the effect of ADP at substoichiometric concentrations. To test the second possibility, we diluted ParM filaments below the apparent ATP critical concentration into either, nucleotide-free buffer, or buffer containing ADP and monitored filament disassembly. Filaments diluted into ADP disassemble at almost twice the rate of filaments diluted into nucleotide-free buffer, indicating that ADP in solution actually increases the rate of filament disassembly (Fig. S3C and S3D). Based on kinetic arguments of Teubner et al. (8), who performed similar assays with conventional actin, we argue that the ADP destabilization is due to nucleotide exchange on monomers at the ends of filaments. Because of this effect we performed all TIRF microscopy and steady-state FRET measurements at ATP concentrations high enough so that the ADP poisoning effect was not seen.

#### **Calculation of monomer association and dissociation rates.**

We determined ParM monomer association and dissociation rates by TIRF microscopy. The growth rates of ATP ParM filaments were constant regardless of protein concentration, implying that the polymer rapidly equilibrates at the steady-state monomer concentration of  $2.3\mu\text{M}$ . We confirmed this rapid equilibration using our FRET polymerization assay (Fig. S3B). To calculate the monomer association rates, we measured filament lengths frame-by-frame in time-lapse sequences. We then divided filament lengths (in pixels) by the pixel size ( $7.465\text{ pixels/micron}$ ) to obtain the length in

microns. We then converted this value to number of monomers in the filament by dividing this value by the length increment of a monomer adding to a ParM filament end ( $24.5\text{\AA}$  – ParM monomers are  $49\text{\AA}$  but each filament is composed of two stranded offset by approximately half the length of a monomer ( $l$ )). As the rate of filament elongation can be represented as  $d(\text{length in monomers})/dt = k^+[\text{free monomer}][\text{single filament}]$ , and the polymer has equilibrated to the critical concentration of  $2.3\mu\text{M}$ ; the on rate ( $k^+$ ) for ATP-ParM monomers onto filaments can be estimated as  $k^+ = (d(\text{length in monomers})/dt)/2.3\mu\text{M}$ . Filament lengths were measured as a function of time and the resultant rate of growth was divided by two (since filaments elongate in a symmetrical, bidirectional manner). To verify the bidirectional polymerization we also measured the distance from stationary fiducial marks within the filament to each end. Both methods yielded similar results. We measured the depolymerization rate of filaments in a similar manner and calibrated the data using the same pixels to subunits conversions as above.

The E148A mutant polymerizes with a slower nucleation rate, especially at low concentrations, and hence we were able to examine the  $d(\text{length in monomers})/dt = k^+[\text{free monomer}][\text{single filament}]$  relationship (9) of the concentration of [free monomer] to the growth rate  $k^+$  (Fig. S4D). Length measurements were taken of filaments growing bidirectionally and this rate divided by two. This data yielded an on rate very close to that of ATP ParM growth rates ( $3.9\mu\text{M}^{-1}\text{sec}^{-1}$  for E148A vs  $5.3\mu\text{M}^{-1}\text{sec}^{-1}$  for ATP-ParM).

### **ParM mutants defective in ATP hydrolysis.**

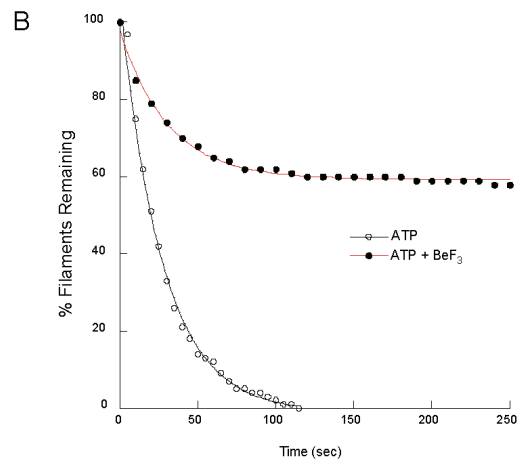
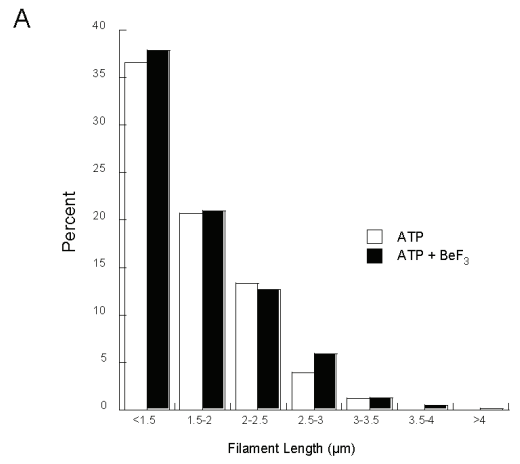
ParM is a potentially important tool for studying actin biochemistry, as the chemical mechanism of ATP hydrolysis by actin is not well understood. Vorobiev *et al* proposed a mechanism for ATP hydrolysis in which Q137 and H161 residues of conventional actin coordinate a catalytic water that makes an in-line attack on the  $\gamma$ -phosphate of the bound ATP (10). These mutations have a negative effect on yeast cell growth and their effect on ATP hydrolysis has never been tested. Alignment of the active sites of ADP actin and ADP ParM indicate that several residues are spatially conserved (Fig S4A). The positions E148 and D177 of ParM superimpose with the Q137 and H161 residues of actin. We generated mutations in ParM at equivalent positions, recovered the proteins and studied their polymerization and nucleotide hydrolysis activities.

Mutation of glutamic acid 148 to alanine in ParM abolishes ATP hydrolysis but does not affect filament elongation supporting the hypothesis that this residue plays a key catalytic role in hydrolysis of ATP by members of the actin superfamily (10). Mutation of aspartic acid 177 to alanine fails to abolish ATPase activity and significantly inhibits polymerization. The critical concentration for polymerization of the D177A mutant in ATP increases from 2.3  $\mu$ M to 12  $\mu$ M (7). We conclude that D177 is not specifically required for ATP hydrolysis and that mutation of this residue generally destabilizes the fold of the protein. Attempts to simultaneously mutate E148 and D177 to the equivalent residues of actin yielded an unfolded protein that would not polymerize. Although mutation of D170 has been used previously to study the role of nucleotide binding and hydrolysis in ParM polymerization, it does not abolish ATP hydrolysis (11). Based on crystal structures of conventional actin and ParM, this residue corresponds to D154 in actin, a residue thought to be involved more in coordination of  $Mg^{2+}$  than in hydrolysis

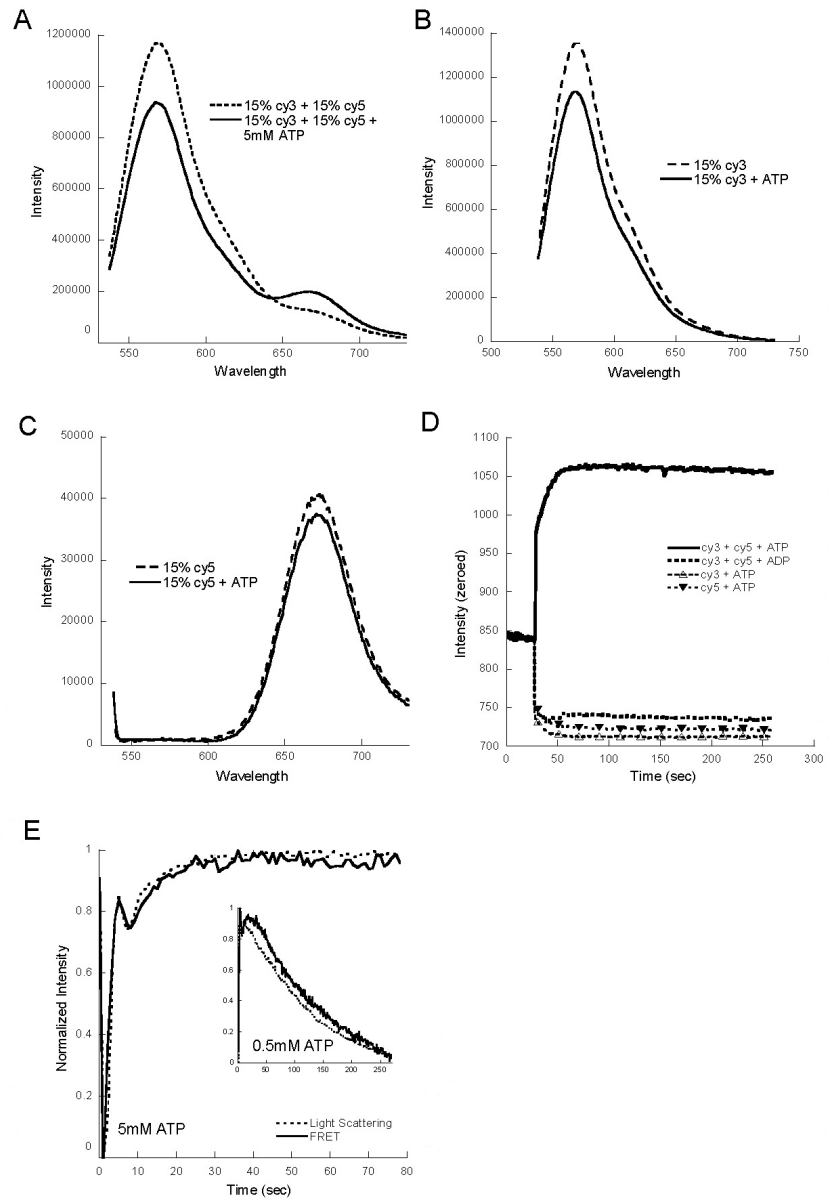
*per se*. In our hands this mutation exhibited significantly perturbed polymerization dynamics (7).

1. F. van den Ent, J. Moller-Jensen, L. A. Amos, K. Gerdes, J. Lowe, *Embo J* **21**, 6935 (Dec 16, 2002).
2. D. W. Pierce, R. D. Vale, *Methods Cell Biol* **58**, 49 (1999).
3. S. S. Rosenfeld, E. W. Taylor, *J Biol Chem* **259**, 11920 (Oct 10, 1984).
4. E. Shacter, *Anal Biochem* **138**, 416 (May 1, 1984).
5. J. Moller-Jensen, R. B. Jensen, J. Lowe, K. Gerdes, *Embo J* **21**, 3119 (Jun 17, 2002).
6. D. L. Taylor, J. Reidler, J. A. Spudich, L. Stryer, *J Cell Biol* **89**, 362 (May, 1981).
7. Data not shown.
8. A. Teubner, A. Wegner, *Biochemistry* **37**, 7532 (May 19, 1998).
9. K. J. Amann, T. D. Pollard, *Proc Natl Acad Sci U S A* **98**, 15009 (Dec 18, 2001).
10. S. Vorobiev *et al.*, *Proc Natl Acad Sci U S A* **100**, 5760 (May 13, 2003).
11. R. B. Jensen, K. Gerdes, *J Mol Biol* **269**, 505 (Jun 20, 1997).

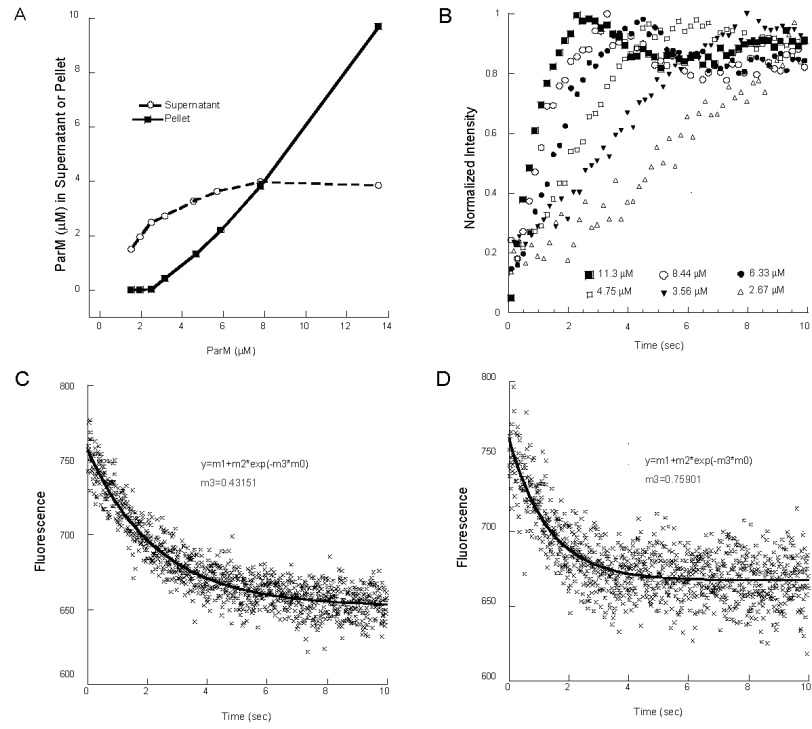
# Supplementary Figure 1



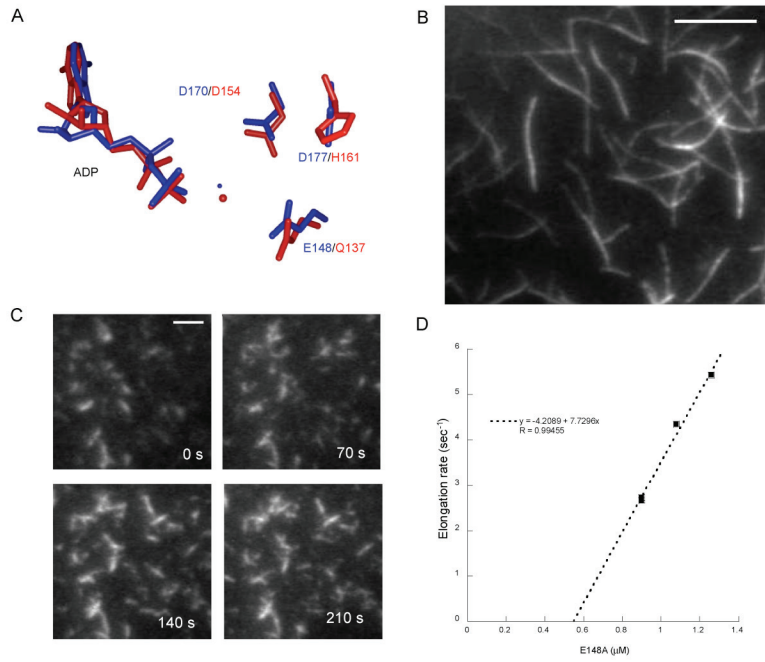
## Supplementary Figure 2



### Supplementary Figure 3



## Supplementary Figure 4





## Supplementary Figure Legends

### Supplementary Figure 1

- (A) The length distributions of ParM filaments polymerized in ATP is identical to that of filaments polymerized in ATP + BeF<sub>3</sub>. Lengths of filaments were measured from single frames of time-lapse movies of ParM polymerized in the presence of ATP (10mM) or in the presence of ATP (10mM) + BeF<sub>3</sub> (0.8mM).
- (B) Survival curves of ParM filaments polymerized in ATP or ATP + BeF<sub>3</sub>. We chose 100 random filaments from individual frames of time lapse TIRF microscopy and followed them until they disappeared from the field. In the presence of ATP alone, none of the filaments survived beyond 120 seconds. Suppression of dynamic instability by addition of BeF<sub>3</sub> results in survival of 60% of the filaments beyond 250 seconds. The filaments that disappear in the presence of BeF<sub>3</sub> all disappear in a single step from one frame to the next, indicating that the filament has floated out of the plane of the evanescent wave. In the presence of ATP alone the majority of the filaments shorten from one or both ends over multiple frames before disappearing.

### Supplementary Figure 2

- (A) Cy3- and Cy5-labeled ParM generate a resonance energy transfer in the ParM filament. A solution of 15μM ParM doped with 15% Cy3 ParM and 15% Cy5 ParM in Buffer F was prepared. 95μL of this sample was placed in a cuvette and either 5μL of 100mM ATP (5mM final) or 5μL of water was added. After 30 seconds, the sample was illuminated at 514nm and wavescans taken. Note that

upon addition of ATP there is an increase in the Cy5 emission between 650-700nm and a decrease in Cy3 emission at the 570nm peak.

- (B) Identical conditions were used as in A, except that the sample contained only Cy3 (15% doping).
- (C) Identical conditions were used as in A, except that the sample contained only Cy5 (15% doping).
- (D) Test of FRET assay for polymerization. 95 $\mu$ L of 13  $\mu$ M ParM, containing either Cy3-labeled ParM, Cy5-labeled ParM, or both, was added to a cuvette and the resultant FRET signal measured. At 25 seconds 5 $\mu$ L ADP (100mM) or ATP (100mM) was added to the reaction.
- (E) The FRET signal overlays light scattering curves of ParM polymerization. 10 $\mu$ M FRET labeled ParM was combined with either 5mM or 0.5mM ATP (inset) with a rapid mixer and the FRET or 90°-light scattering (at 310nm) signal recorded from the same sample (K2 fluorimeter, ISS). All values are normalized.

### **Supplementary Figure 3**

- (A) ParM displays an apparent ATP critical concentration as assayed by high-speed centrifugation and pelleting. Serially diluted ParM was polymerized by addition of 5mM ATP and pelleted using an ultracentrifuge. Plotted are the quantities of supernatant and pellet protein determined using gel densitometry.
- (B) ParM polymerization displays a concentration-dependent lag time. We mixed FRET-labeled ParM at the indicated concentrations with 5mM ATP using a rapid mixer and measured FRET. Conditions: excitation: 514nm, emission: 690nm

Buffer: 100mM KCl, 30mM Tris HCl pH 7.5, 1mM DTT, 1mM MgCl<sub>2</sub>. Signals were then normalized to their minimal and maximal values.

- (C) ParM depolymerizes in an exponential fashion. 4 $\mu$ M FRET-labeled ParM was polymerized in 2mM ATP for 5 minutes, then diluted 2-fold to 2 $\mu$ M (below the measured critical concentration) into Buffer F using a rapid mixer.
- (D) ADP actively destabilizes ParM filaments. Identical conditions were used as in (E), except that the protein was diluted into Buffer F containing 1mM ADP.

#### **Supplementary Figure 4**

- (A) ParM and actin share spatially-conserved residues in the ATP-binding pocket. We superimposed the atomic structures of the active sites of ADP-actin and ADP-ParM. Red atoms and labels are from the actin structure, blue atoms and labels are from ParM.
- (B) The hydrolysis-deficient E148A ParM mutant forms long, stable filaments. TIRF image of 900nM 10% Alexa-488-labeled E148A ParM polymerized with 10mM ATP. Scale bar indicates 10 microns.
- (C) Sub-stoichiometric concentrations of E148A stabilize ParM filaments and block catastrophic filament disassembly. TIRF time-lapse frames of 2.7 $\mu$ M 10% Alexa-488-labeled ParM (20% E148A, 80% wild-type) polymerized with 10mM ATP. Scale bar indicates 5 microns.
- (D) The elongation rate of E148A ParM is the same as wild-type ParM. We plotted the elongation rate of Alexa-488-labeled E148A ParM, as measured by TIRF, versus protein concentration. The slope of the graph is twice the value of  $k^+$  (as

the polymer elongates bidirectionally), and the x-intercept is the critical concentration.

### Supplementary movies.

All movies are available online at

<http://www.sciencemag.org/cgi/content/full/sci;306/5698/1021/DC1>

All movies are time-lapse, total internal reflection fluorescence (TIRF) microscopy sequences. Filaments are labeled with 10% Alexa-488 and polymerized in Buffer F with 10mM nucleotide.

1. Polymerization of a single ParM filament in the presence of AMPPNP. Images were collected at 10-second intervals.
2. A field of AMPPNP ParM filaments. Images were collected at 10-second intervals.
3. Polymerization of a single ParM filament in the presence of ATP. Images were collected at 10-second intervals.
4. A montage of individual ATP ParM filaments elongating and undergoing catastrophic disassembly. Growing ends of filaments are indicated by green marks, while ends of shrinking filaments are indicated by red marks. Each sequence is shown twice in succession. Images were collected at 5-second intervals.
5. A field of ATP ParM filaments. Images were collected at 5-second intervals.
6. Behavior of ATP ParM filaments in the presence of 0.8mM BeF<sub>3</sub>. Images were collected at 10-second intervals.
7. Polymerization of 100% E148A ParM filaments. Images were collected at 10-second intervals.

8. Polymerization of Alexa-488-labeled wild-type ParM in the presence of 20% unlabeled, non-hydrolyzing E148A mutant. Images were collected at 10-second intervals.
9. Comparative movie showing 4 fields of ParM filaments polymerized under different conditions. ParM was polymerized with ATP, ATP + BeF<sub>3</sub>, AMPPNP, or ATP ParM doped with 20% E148A. N.B. Because ATP ParM filaments are so much more dynamic, we collected the ATP images at a 3-fold faster rate. The movies have been adjusted for this difference so that their timescales are identical.

## Materials and Methods

### Expression and purification of ParM:

DNA encoding ParM was PCR-amplified from the R1-19 plasmid using primers that, when translated, add five additional amino acids (GSKCK) to the C-terminus. The KCK sequence was appended to enable covalent attachment of fluorescent probes containing sulfhydryl-reactive functional groups. The PCR product was cloned into a pet-11a vector and sequenced. BL21 cells were transformed, grown at 37°C, and induced with 1mM IPTG at an OD600 of 1.0 for 4 hours. Protein was purified as described (1), dialyzed into Buffer F (100mM KCl, 30mM Tris HCl pH 7.5, 1mM DTT, 1mM MgCl<sub>2</sub>), and gel filtered over a Superdex 75 column equilibrated in Buffer F. Peak fractions were frozen in 20% glycerol.

### Expression and purification of ParM mutants:

ParM hydrolysis mutants were generated by Quickchange (Stratagene, La Jolla, CA) on the above construct. As the mutant proteins would polymerize directly out of the ATP in cell lysates, we modified the wild-type ParM purification protocol to induce depolymerization. Briefly, we lysed cells in Buffer F + 2mM EDTA. We then clarified the extract by high-speed centrifugation, and treated the extracts with 2 times with 0.1 volume of Dowex AG 1-X2 resin (Sigma Chemicals, St Louis MO) at pH 7.5 to remove residual nucleotide. This sample was spun at 38,000 RPM in a Beckman Ti-45 for 1 hour to remove any residual resin and aggregates. ParM polymerization was induced by addition of 10mM ATP and 10mM MgCl<sub>2</sub>. We then pelleted ParM polymer by centrifugation as above and resuspended the pellets in Buffer F + 40mM EDTA. We

briefly sonicated the resuspended ParM to fragment filaments and promote depolymerization and then incubated the protein 2 times with 0.1 volume of Dowex AG 1-X2 resin on ice. The sample was centrifuged as above, and the supernatant dialyzed 3 times against 1L of Buffer F containing a dialysis cassette with 25,000 units of apyrase in the same container. For storage we added 20% glycerol and snap froze aliquots of ParM in liquid nitrogen and stored them at -80°C.

**Labeling of ParM with fluorescent dyes:**

Glycerol and DTT were removed by a PD10 salt exchange column equilibrated in Buffer F without DTT. For labeling we added a 5-fold molar excess of dye to protein and incubated for 10 minutes at 25°C. We quenched the reaction with 10mM DTT and removed free dye by gel filtration on G25 resin. Samples were frozen down following addition of 0.2M sucrose. Average labeling efficiency for samples used in this study was 100±15%.

**Estimation of steady-state monomer (critical) concentration by high-speed pelleting:**

Unlabeled ParM was serially diluted into Buffer F and concentrations determined by absorbance at 280nm. Protein was polymerized by addition of 5µM ATP, and immediately spun in a TLA 100.4 at 100,000xg for 15 minutes at 25°C. Pellets were resuspended in Buffer F and equal volumes of supernatant and pellet samples were combined with sample buffer, boiled, and separated by gel electrophoresis on 4-12% poly-acrylamide gradient gels. Gels were stained with Comassie Brilliant Blue and quantitated using NIH ImageJ (<http://rsb.info.nih.gov/ij/>). Concentrations were calibrated



based on absorbance at 280nm or actin standards loaded on the same gel. Both methods yielded similar results.

### **FRET and light scattering assays of ParM polymerization/depolymerization**

#### **kinetics:**

FRET-labeled samples were prepared by doping unlabeled ParM in Buffer F with 15% Cy3- and 15% Cy5-labeled ParM. Concentrations and percentage dopings were confirmed by absorbance at 280, 552, and 650nm. FRET measurements of polymerization were made using a digital K2 Fluorimeter (ISS, Champagne IL) at an excitation wavelength of 514nm and emission wavelength of 690nm. Kinetic assays were conducted by mixing the FRET-labeled ParM with ATP in Buffer F using a SFA-20 rapid mixer (Hi-Tech). Where indicated, the zero value of the FRET signal was taken as the fluorescence of the first 200 msec of the reaction following addition of ATP. The concentration of filamentous ParM was calculated by taking samples at known concentrations and polymerizing with saturating amounts of ATP. Under these conditions, the fluorescence corresponds to the total concentration of protein minus the critical concentration. Right angle light scattering was conducted under identical conditions using an excitation wavelength of 314nm.

#### **Fret assays determinations of the critical concentration:**

FRET-labeled ParM was serially diluted into Buffer F, and the concentrations verified by absorbance at 280nm. We placed 95 $\mu$ L aliquots in a fluorimeter cuvette. We then excited each sample at 514nm and measured fluorescence at 690nm. For each sample we

measured fluorescence in the absence of ATP and then added 5  $\mu$ L of 100 mM ATP; allowed the sample to equilibrate for 5 minutes and measured the fluorescence of the polymerized ParM. We corrected for dilution and subtracted the baseline fluorescence of nucleotide-free ParM from that of ATP ParM and plotted this value as a function of ParM concentration. The critical concentration was taken as the x intercept of this plot.

**Stabilization of ParM filaments by substoichiometric concentrations of E148A mutant:**

Cy3-ParM and Cy5-E148A were prepared as above, diluted to 5.1  $\mu$ M in Buffer F, and combined at the indicated ratios. ATP was added to a final concentration of 10mM, samples were incubated for 10 minutes and then spun in a TLA 100.4 at 100,00xg for 15 minutes at 25°C. The supernatant and pellet samples were treated as above, and loaded onto a 4-12% SDS-PAGE gradient gel. We quantitated Cy3 and Cy5 fluorescence using a scanning fluorescence imager (Typhoon, Molecular Dynamics, Sunnyvale, CA) with excitation/emission filter pairs of 532nm/580nm and 633nm/670nm respectively. Supernatant and pellet samples were normalized by (fluorescence)/(supernatant fluorescence + pellet fluorescence).

**Total internal reflection fluorescence (TIRF) microscopy:**

The total internal reflection fluorescence microscope used in these studies has been described elsewhere (2). Slides and cover slips were sonicated in 100mM KOH, followed by ethanol for 20 minutes each. After drying, cover slips were treated with .01% poly-l-lysine and washed with 3mL ddH<sub>2</sub>O. ParM protein in Buffer F with 0.6% BSA and 0.8%

methyl cellulose was combined in a 9:1 ratio with 100mM ATP or AMP-PNP directly on a slide and then immediately covered with a cover slip.

**Dual color fluorescence microscopy:**

1 $\mu$ L of 4.3  $\mu$ M Alexa-488-ParM was first mixed with 0.2 $\mu$ L of 100mM AMPPNP. Thirty seconds later, 1 $\mu$ L of 3.1 $\mu$ M Cy3-ParM was added. After 1 minute, the mixture was diluted with 20 $\mu$ L Buffer F and samples were immediately applied to poly-lysine-coated coverslips for fluorescence imaging. Microscopy was performed on an inverted epifluorescence microscope (TE300, Nikon) fitted with a cooled CCD camera (OrcaII, Hamamatsu).

**Determination of ATP on and off rates:**

Gel filtered ParM was diluted to 100nM (for ATP) or 5 $\mu$ M (for ADP) in Buffer F plus 200mM acrylamide (to quench free fluorescent nucleotide derivatives (3)). **Nucleotide dissociation rate constants:** Equal amounts of etheno-ATP or etheno-ADP were added to the protein and equilibrated for 15 minutes. Samples were diluted into 5mM dark ADP or ATP in Buffer F plus 200mM acrylamide using a rapid mixer, and the fluorescence decay measured ( $\epsilon_x = 340$  nm,  $\epsilon_m = 420$  nm) using the K2 Fluorometer. Three reactions were averaged and fit with a single exponential decay to determine the off rate.

**Nucleotide association rate constants:** Samples of nucleotide-free ParM were combined with increasing concentrations of etheno-ATP or etheno-ADP and the fluorescence increase measured as above. Three separate reactions were averaged and fit with a single exponential attack to determine an observed rate constant ( $k_{obs}$ ). We plotted  $k_{obs}$  versus

etheno-nucleotide concentration. The slope of this plot was taken as the nucleotide association rate constant.

### **Measurement of ATP hydrolysis and calculation of hydrolysis rate constant:**

To measure ATP hydrolysis by ParM, we mixed FRET-labeled ParM in Buffer F with ATP containing approximately 20  $\mu$ Cu of  $^{32}$ P- $\gamma$ -ATP (ALT Inc.) in a quenched-flow rapid mixer (RQF-3, KinTek, Austin, TX), incubated for various times and quenched with 2.5M formic acid. We extracted  $^{32}$ P as described by Shacter et al. (4) and quantified radioactivity by scintillation counting. We collected baseline data for all measurements by combining ATP with Buffer F alone. We calibrated the total releasable radioactivity from 200  $\mu$ L of ATP incubated with 1 unit of apyrase for at least 1 hour.

We estimated the rate constant for ATP hydrolysis by three methods. By simply noting that 12.5  $\mu$ M polymeric ParM polymer hydrolyzes 10  $\mu$ M ATP in approximately 10 seconds we obtain a lower bound on the rate constant of 0.08  $\text{s}^{-1}$ . Since polymerization is fast and hydrolysis is a first-order reaction we can also estimate the rate constant from the rate of ATP hydrolysis at the very earliest time points in the reaction. The initial rate of ATP hydrolysis is 2.8  $\mu$ M/sec which yields a rate constant of 0.22  $\text{s}^{-1}$ . To determine a more accurate rate constant for ATP hydrolysis we require an estimate of the instantaneous concentration of polymeric ATP-ParM. For this we constructed a simple mathematical model of a two-state polymer. Three dynamical variables describe monomeric ParM:  $M$  – concentration of nucleotide-free monomers,  $M_T$  – concentration of ATP-monomers, and  $M_D$  – concentration of ADP-monomers. Two dynamical variables describe filament ends:  $E_T$  – the concentration of ATP-capped ends, and  $E_D$  –

the concentration of ends with ADP-monomers. We also considered ATP (T) and ADP (D) concentrations as dynamical variables. The concentration of ATP-ParM polymer is  $P_T$  and ADP-ParM polymer is  $P_D$ . The complete description of polymerization and depolymerization dynamics is given by:

$$\begin{aligned}
d/dt(M) &= k_{D-} * M_D - k_{D+} * M * D + k_{T-} * M_T - k_{T+} * M * T \\
d/dt(M_T) &= - k_{T-} * M_T + k_{T+} * M * T - 3 * k_{nucl} * M_T * M_T * M_T - k_{PT+} * M_T * E_T + k_{PT-} * E_T \\
d/dt(M_D) &= - k_{D-} * M_D + k_{D+} * M * D + k_{PD-} * E_D + 3 * k_{DD} * k_{PD-} * E_D \\
d/dt(E_T) &= k_{nucl} * M_T * M_T * M_T - (1/(1+(k_{PT+} * M_T/k_{hydroly})) * kh * E_T - (1/(1+(k_{PT-}/k_{hydroly}))) * k_{PT-} * E_T \\
d/dt(E_D) &= (1/(1+(k_{PT+} * M_T/k_{hydroly}))) * kh * E_T + (1/(1+(k_{PT-}/k_{hydroly}))) * k_{PT-} * E_T - k_{DD} * k_{PD-} * E_D \\
d/dt(P_T) &= 3 * k_{nucl} * M_T * M_T * M_T + k_{PT+} * M_T * E_T - k_{PT-} * E_T - k_{hydroly} * P_T \\
d/dt(P_D) &= k_{hydroly} * P_T - kc2 * E_D - 2 * k_{DD} * k_{PD-} * E_D \\
d/dt(T) &= - k_{T+} * M * T + k_{T-} * M_T \\
d/dt(D) &= - k_{D+} * M * D + k_{D-} * M_D
\end{aligned}$$

The rate constants are defined by:

parameter	value	definition	source
$k_{D-}$	$0.6 \text{ s}^{-1}$	Dissociation of ADP from ParM monomer	Direct measurement
$k_{D+}$	$0.2 \mu\text{M}^{-1} \text{ s}^{-1}$	Association of ADP with ParM monomer	Direct measurement
$k_{T-}$	$0.01 \text{ s}^{-1}$	Dissociation of ATP from ParM monomer	Direct measurement
$k_{T+}$	$0.2 \mu\text{M}^{-1} \text{ s}^{-1}$	Association of ATP with ParM monomer	Direct measurement
$k_n$	$10^{-4} \mu\text{M}^{-2} \text{ s}^{-1}$	Nucleation rate constant	Model fitting
$k_{PT+}$	$5 \mu\text{M}^{-1} \text{ s}^{-1}$	ATP-ParM association with filament end	TIRF microscopy
$k_{PT-}$	$3.3 \text{ s}^{-1}$	ATP-ParM dissociation from filament end	Calculated from critical concentration
$k_{PD-}$	$64 \text{ s}^{-1}$	ADP-ParM dissociation from filament end	TIRF microscopy
$k_{DD}$	0-0.02	Probability of losing an ADP filament end	Calculated from measured parameters
$k_{hydroly}$	$0.2 \text{ s}^{-1}$	Rate of ATP hydrolysis	Model fitting

We used Berkeley Madonna 8.0.1 $\beta$  (Robert Macey and George Oster, University of California, Berkeley CA) to perform simultaneous fitting of our mathematical model to both polymerization and ATP hydrolysis data. The features of this model that differentiate it from standard models of actin filament assembly are: (1) it includes different rate constants for dynamics of ATP and ADP ends, (2) it keeps track of the concentration of both ATP- and ADP-ParM filament ends, (3) it allows conversion of ATP-ParM ends to ADP-ends by either ATP hydrolysis on the terminal subunit or uncovering of an ADP subunit by loss of an ATP monomer, (3) it assumes that ADP filament ends disassemble at a constant rate without rescue, and (4) it assumes an

exponential filament length distribution and keeps track of filament ends lost due to complete depolymerization. A more complete description of this model will be published elsewhere.

The model has only two floating parameters – the rate constants for nucleation and ATP hydrolysis – and fits both polymerization and hydrolysis data sets well. The model even captures the enigmatic hump in the polymerization data, suggesting that it is an accurate description of ParM polymerization, ATP hydrolysis, and the connection between them. From this analysis we determine a rate constant for ATP hydrolysis of  $0.2 \text{ s}^{-1}$ , which agrees well with our other estimates.

## **Chapter 4**

**Reconstitution of DNA segregation driven by assembly of a prokaryotic actin  
homolog.**

**Ethan C. Garner, Chris Campbell, Douglas Weibel,  
R. Dyche Mullins**

**Published: Mar 2, 2007, *Science*, 315(5816):1270-4.**

## Abstract

Multiple unrelated polymer systems have evolved to partition DNA molecules between daughter cells at division. To better understand polymer-driven DNA segregation, we reconstituted the 3-component segregation system of the R1 plasmid using purified components. We found that the ParR/*parC* complex can construct a simple bipolar spindle by binding the ends of ParM filaments, inhibiting dynamic instability, and acting as a ratchet, permitting incorporation of new monomers and riding on the elongating filament ends. Under steady-state conditions the dynamic instability of unattached ParM filaments provides the energy required to drive DNA segregation.



## Results and Discussion

To ensure fidelity of gene transmission, DNA molecules must be evenly distributed among daughter cells before division. Eukaryotes harness the polymerization of tubulin to drive alignment and segregation of chromosomes (1); chromosome segregation in some eubacteria requires assembly of actin-like filaments (2, 3); and some extra-chromosomal DNA elements have evolved their own polymer-based DNA segregation machinery (4, 5). Plasmid R1 is a large (100 kb), low-copy plasmid with segregation machinery encoded by the *par* operon (6, 7). This operon is composed of three elements, *parC*, *parR*, and *parM* (6). *parM* encodes an actin-like protein that assembles into dynamically unstable filaments (8). *parR* encodes a protein that binds cooperatively to sequence repeats within *parC*, forming a complex that binds ParM filaments (9). It has been proposed that products of the *par* operon assemble into a bipolar spindle-like structure whose elongation drives plasmid segregation (9), but how these components assemble and how they convert the free energy of ParM polymerization into useful work remain unknown.

By atomic structure, ParM is similar to actin (10) but by filament assembly dynamics, ParM is distinguished from actin by three important properties: (i) rapid, rather than slow, spontaneous nucleation, (ii) symmetrical, bidirectional elongation rather than polarized growth, and (iii) dynamic instability (the tendency to switch spontaneously (11) between phases of steady elongation and rapid shortening), rather than steady-state treadmilling (8). The combination of these kinetic parameters results in a steady-state population of short (~1.5µm) and unstable (lifetime ~ 20 sec) ParM filaments (8).

To understand how ParR and *parC* harness filament assembly to segregate DNA, we purified all three components and tested their ability to self-assemble in vitro. We expressed and purified ParM and ParR proteins from *E. coli* (Fig. S1). We attached fluorescent (Cy-3-labeled) DNA containing the *parC* sequence to 350nm spherical beads. We then mixed the *parC*-coupled microspheres with ParR, added fluorescently labeled (Alexa-488) ParM, and induced filament assembly by adding ATP.

ParM filaments formed small radial arrays surrounding isolated *parC* beads (Fig. 1A), structures reminiscent of microtubule asters formed around isolated centrosomes (12). Aster formation required ATP, ParR (Fig. S2A), and DNA containing the *parC* sequence (Fig. S2B). Asters were dynamic, with filaments growing and shrinking from the surface of the bead, and grew to a maximum radius of 3 $\mu$ m (Fig. 1B, Movie S1), similar to the maximum lengths of individual ParM filaments in solution (8). In the presence of the non-hydrolyzable ATP analog, Adenylylimidodiphosphate (AMPPNP) astral ParM projections grew much longer (Fig. 1C, Fig. S3, Movie S2), indicating that the dynamic instability of ParM limited filament length even when one end of the filament was bound to the ParR/*parC* complex.

In addition to dynamic asters, ParM filaments also formed long, stable bundles connecting pairs of *parC* beads (Fig. 1D-G), similar to bipolar structures previously observed in vivo (7). The bundles and attached beads moved as a single unit with fluid flow, indicating that ParM filaments were tightly attached to the ParR/*parC* complex. By

electron microscopy we observed *parC* beads connected by ParM bundles of varying thickness. We traced individual filaments from one *parC* bead to the other (Fig. 1E), indicating that both ends of the ParM filament interacted with the ParR/*parC* complex. In time-lapse movies, the bivalently-attached ParM bundles elongated at a constant rate, pushing *parC* beads in opposite directions (Fig. 1D, 1F, Movies S3-4) over long distances (>120 $\mu$ m). Thus ParM, ParR, and *parC* are sufficient to form a bipolar, DNA-segregating spindle. In addition, multiple *parC* beads often interacted to form multipolar linear chains and polygons of ParM bundles (Fig. 1G, Movies S5-6), structures that also expanded equilaterally as each bundle elongated at the same rate.

The fact that we observed long, stable ParM filaments only between pairs of *parC* beads argues that both ends of each filament are stabilized against catastrophic disassembly by interaction with the ParR/*parC* complex. This is supported by the observation of a “search-and-capture” (13) process of spindle formation: when two unconnected ParM asters come into proximity, they stabilize a filament bundle whose elongation pushes the asters apart (Fig. 2A, Fig. S4, Movies S7-8). We tested whether bipolar attachment was required for stabilization by using laser irradiation to cut through ParM spindles. After cutting, both severed ends of the bundle depolymerized back to the *parC* beads (Fig. 2B, Fig. S5, Movies S9-10). This requirement for bipolar stabilization of ParM spindles provides an explanation for the apparent plasmid counting observed *in vivo*, where ParM spindles occur only in cells containing two or more plasmids (9).

To determine whether the R1 spindle was sufficient to find the long axis of a bacterium-sized space, we assembled spindles in microfabricated channels of various shapes.

Spindles always aligned with the long axis of the channel and pushed *parC* beads in opposite directions (Fig. 2C, Movie S11), demonstrating that orientation of R1 spindles can occur without cellular landmarks. Spindles elongated freely until they encountered resistance. Elongation stalled at the ends of the channels and slowed at bends. Thus the R1 spindle could find the long-axis of a rod-shaped cell by a simple Brownian ratchet-type mechanism.

We next used photobleaching and speckle microscopy to determine where new ParM monomers incorporated into the R1 spindle. We first used low-intensity laser irradiation to photobleach pairs of reference marks onto elongating spindles (Fig. 3A, Fig. S6, Movie S12). In all cases ( $n=6$ ) the distance between the two bleached marks did not change with time, while the distance between each mark and the nearest *parC* bead increased at a constant rate (Fig. 3B). We never observed recovery of fluorescence within a bleached zone, suggesting: (1) that no polymerization took place in the middle of the ParM bundle; and (2) that individual filaments did not slide past each other. Speckle microscopy (14) of elongating spindles indicated that monomers incorporated exclusively at the surface of *parC* beads (Fig. 3C, Movies S13-14).

Interaction with the ParR/*parC* complex did not affect the rate of ParM filament growth. From the photobleaching and speckling experiments we determined that filaments within a spindle elongate at a rate of  $11.6 (\pm 1.7; n=5 \text{ ends})$  monomers/second. From the elongation rate and steady-state monomer concentration of  $2.3\mu\text{M}$ (15) we calculate a rate

constant for elongation of bead-attached ParM filaments of  $5 \mu\text{M}^{-1}\text{sec}^{-1}$ , identical to the rate constant for elongation of free ParM filaments (8).

In ParM mutants defective in ATP hydrolysis the critical concentration for assembly is  $0.6 \mu\text{M}$  (8). This is the free monomer concentration above which ATP ParM filaments elongate and below which they shorten. The critical concentration of ADP ParM filaments is more than 200-times higher ( $>120 \mu\text{M}$ ), and this nucleotide-dependent increase is the basis for dynamic instability of ParM filaments. At steady state, in the presence of ATP, the rate of filament nucleation is balanced by the rate of filament catastrophe, and the combination of growing and shrinking filaments produces a steady-state monomer concentration of  $2.3 \mu\text{M}$ . Beneath  $2.3 \mu\text{M}$  no filaments are detectable by fluorescence microscopy, FRET, or high-speed pelleting (8).

To determine how binding to the ParR/*parC* complex affects the critical concentration of ParM filaments we investigated the concentration dependence of R1 spindle formation. At concentrations above  $2.3 \mu\text{M}$ , ParM formed numerous dense and stable spindles connecting pairs of *parC* beads (Fig. 4A). ParM formed spindles between beads below  $2.3 \mu\text{M}$  but their frequency and lifetime decreased with decreasing ParM concentration. Below  $0.6 \mu\text{M}$  ParM failed to form any detectable spindles, even between *parC* beads in close contact. Thus, interaction with the ParR/*parC* complex stabilized ParM filaments down to, but not beneath the ATP critical concentration of  $0.6 \mu\text{M}$ , presumably because the ParR/*parC* complex simply inhibits dynamic instability.

One consequence of our results is that the energy to segregate *parC* beads must be supplied by dynamic instability of unattached ParM filaments. For polymerization to perform useful work, the monomer-polymer balance at the load must be kept away from equilibrium (16). We find that ParM filaments in the spindle are stabilized to the ATP critical concentration (0.6 $\mu$ M) (Fig. 4A), yet elongate at a rate determined by the steady-state monomer concentration of 2.3 $\mu$ M (Fig. 3B), a concentration that is maintained by dynamic instability of unattached ParM filaments (8).

To demonstrate this directly we varied the energy difference between attached and unattached filaments by adding different ratios of ATP and AMPPNP to our reconstituted DNA segregation system. In 100% AMPPNP the ParR/*parC*-attached and unattached filaments had the same critical concentration (0.6  $\mu$ M), and the system quickly reached equilibrium ( $\sim$  2 minutes) with *parC* beads surrounded by a small, non-dynamic shell of ParM filaments (Fig. 4B). Reestablishing an energy difference by adding small amounts of ATP produced sustained ParM polymerization at the bead surface. In 5% ATP and 95% AMPPNP, slow-growing, stable, monopolar tails assembled on the surface of large *parC* beads, propelling them through the medium at a constant rate for up to 2 hours (Fig. 4C, Movies S15-16). By using two colors of labeled ParM, added at different times (Fig. 4D), we found that filament elongation occurred exclusively on ParR/*parC* associated ends and not on free ends. Hence, the unattached filament ends are at steady state, while ParR/*parC*-associated ends elongate in a hydrolysis-dependent manner. The elongation rate of stabilized tails increased with the proportion of hydrolysable ATP (Fig. 4E),

demonstrating that the energetic difference driving bead motility was proportional to the amount hydrolysis capable monomer that could be stabilized by the ParR/*parC* complex.

In response to evolutionary pressure, the R1 plasmid has evolved a self-contained, three-component system to ensure its segregation. All key functions of the R1 spindle require dynamic instability of ParM filaments. Dynamic instability enables unbound filaments to turn over without disassembly factors (8). Filaments stabilized at one end by ParR/*parC* can search for additional plasmids (Fig. S8, Movie S17); filaments bound at both ends are stabilized against dynamic instability, forming a productive spindle. Finally, the dynamic instability of unbound filaments provides the excess monomer to drive elongation of the stabilized filaments within the spindle.

### **Funding Support**

This work was supported by grants to RDM from the NIH (RO1GM61010 and RO1GM675287); the Sandler Family Supporting Foundation; and the UCSF/UCB Nanomedicine Development Center.

1. S. Inoue, H. Sato, *J Gen Physiol* **50**, Suppl:259 (Jul, 1967).
2. Z. Gitai, N. A. Dye, A. Reisenauer, M. Wachi, L. Shapiro, *Cell* **120**, 329 (Feb 11, 2005).
3. T. Kruse *et al.*, *Genes Dev* **20**, 113 (Jan 1, 2006).
4. K. Gerdes, J. Moller-Jensen, R. Bugge Jensen, *Mol Microbiol* **37**, 455 (Aug, 2000).

5. G. E. Lim, A. I. Derman, J. Pogliano, *Proc Natl Acad Sci U S A* **102**, 17658 (Dec 6, 2005).
6. K. Gerdes, S. Molin, *J Mol Biol* **190**, 269 (Aug 5, 1986).
7. J. Moller-Jensen, R. B. Jensen, J. Lowe, K. Gerdes, *Embo J* **21**, 3119 (Jun 17, 2002).
8. E. C. Garner, C. S. Campbell, R. D. Mullins, *Science* **306**, 1021 (Nov 5, 2004).
9. J. Moller-Jensen *et al.*, *Mol Cell* **12**, 1477 (Dec, 2003).
10. F. van den Ent, J. Moller-Jensen, L. A. Amos, K. Gerdes, J. Lowe, *Embo J* **21**, 6935 (Dec 16, 2002).
11. T. Mitchison, M. Kirschner, *Nature* **312**, 237 (Nov 15-21, 1984).
12. M. Moritz *et al.*, *J Cell Biol* **130**, 1149 (Sep, 1995).
13. T. E. Holy, S. Leibler, *Proc Natl Acad Sci U S A* **91**, 5682 (Jun 7, 1994).
14. C. M. Waterman-Storer, A. Desai, J. C. Bulinski, E. D. Salmon, *Curr Biol* **8**, 1227 (Nov 5, 1998).
15. See supporting data on *Science Online*.
16. J. A. Theriot, *Traffic* **1**, 19 (Jan, 2000).
17. We thank O. Akin and M. Quinlan for assistance with bead motility assays. We thank Q. Justman and A. Murray for helpful discussions. We are grateful to S. Layer for continued advice and inspiration.





Figure 1

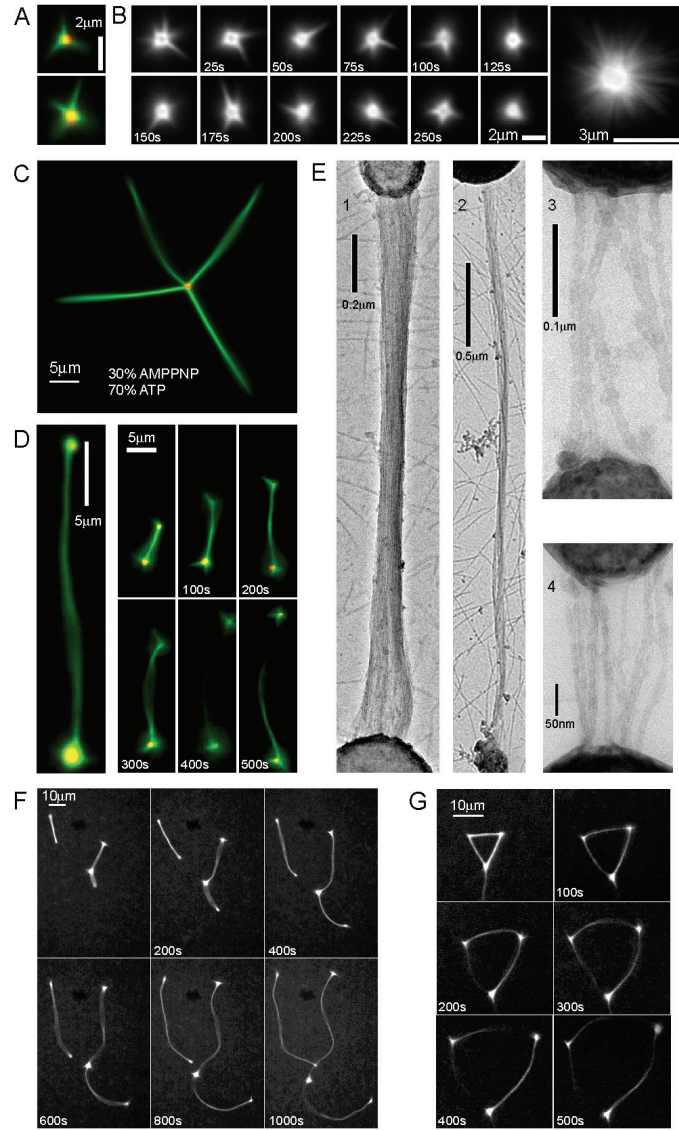


Figure 2

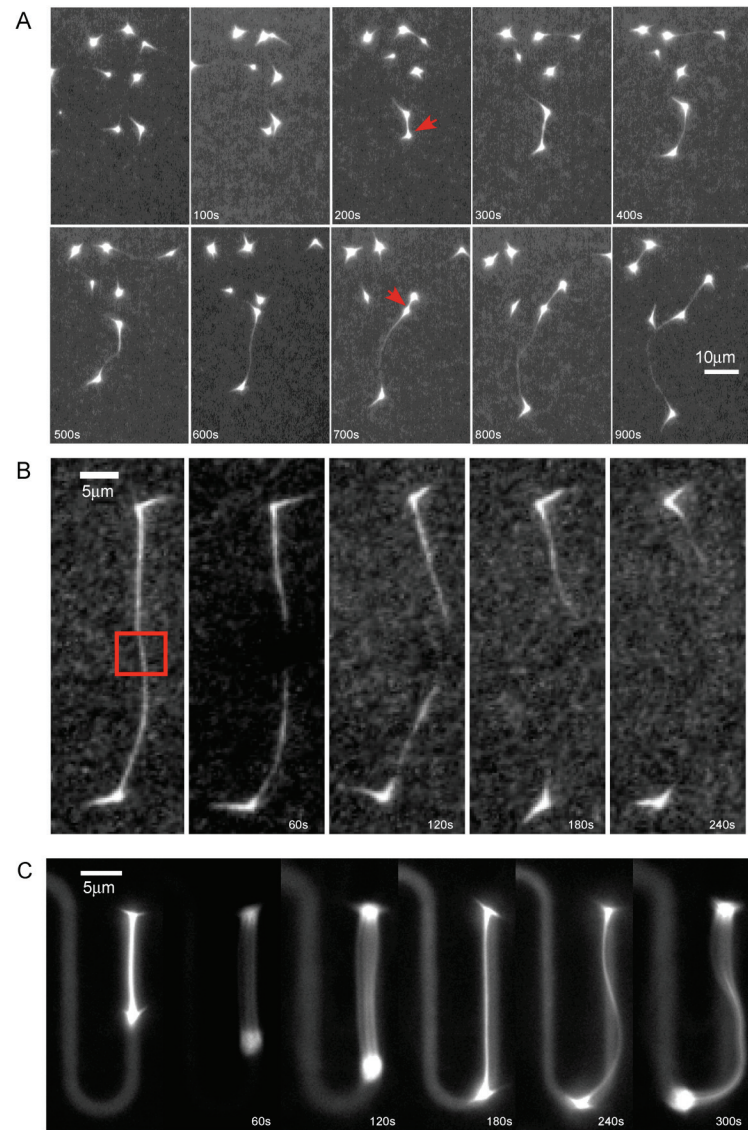


Figure 3

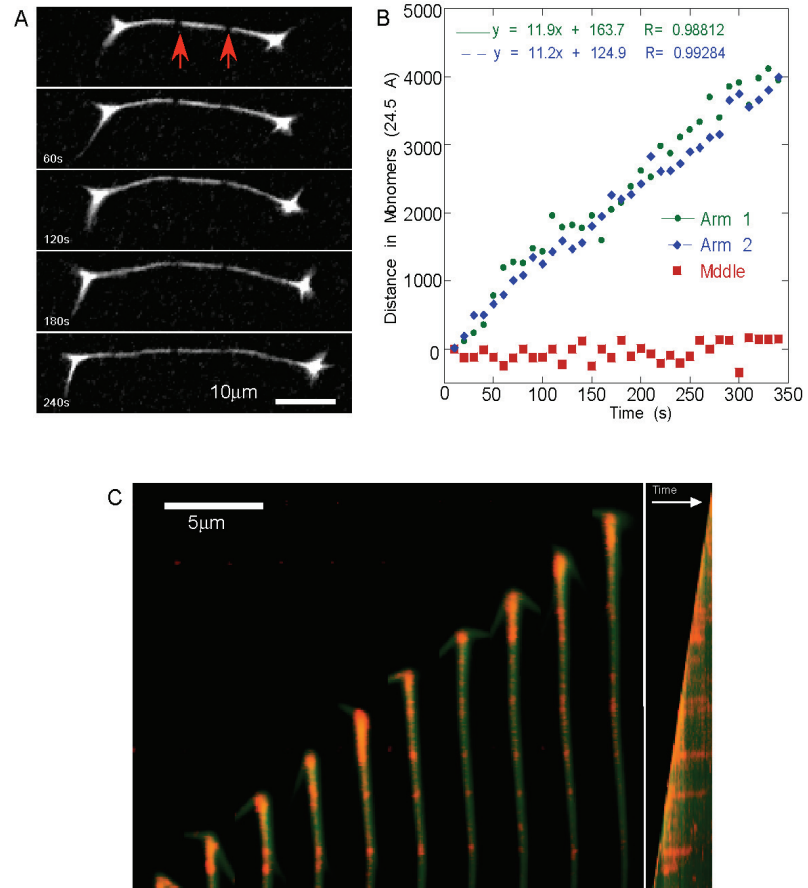
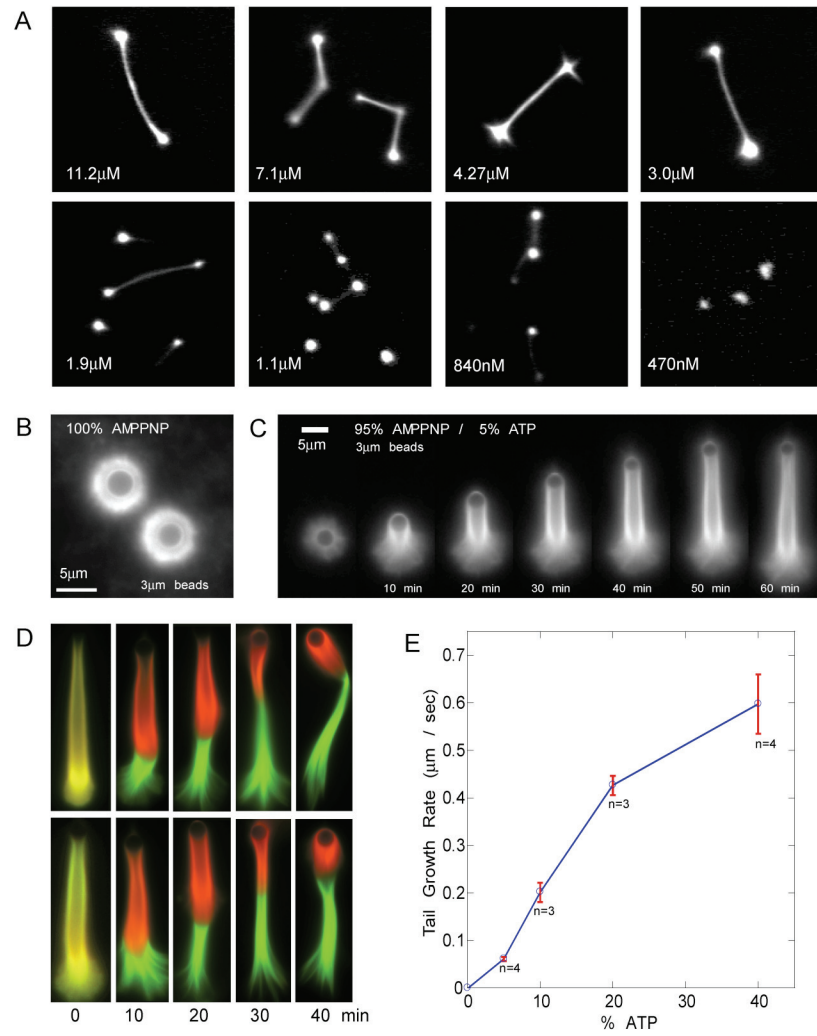


Figure 4.



**Fig. 1. In vitro reconstitution of the R1 plasmid spindle.**

(A) Individual ParR/*parC*-coated beads with radiating fluorescently labeled ParM asters (red is Cy3-labeled DNA, green is Alexa-488-labeled ParM).

(B) Left: Time-lapse sequence of an Alexa-488-labeled ParM aster. Right: Maximum intensity projection of the time-lapse sequence, illustrating fall off in fluorescence at 3 $\mu$ m.

(C) Inhibition of ParM dynamic instability with AMPPNP produces significantly larger asters.

(D) Two-color images and time-lapse sequence of bipolar ParM spindles segregating ParR/*parC* coated beads.

(E) Individual ParM filaments run from bead to bead. Electron microscopy of negatively stained R1 spindles.

(F) Time lapse series of bipolar spindle elongation.

(G) Elongation of a multipolar ParM structure.

**Fig. 2. ParM filaments are stabilized when bound at each end by the ParR/*parC* complex.**

(A) ParM spindles form by “search and capture”. Sequence showing isolated ParM asters forming bipolar spindles that subsequently push the beads apart. Red arrows indicate capture events.

(B) ParM filament bundles are stabilized at both ends by interaction with ParR/*parC* beads.

Cutting a ParM spindle by laser irradiation (red box) results in depolymerization of severed ends.

(C) The R1 spindle finds the long axis of a channel. Time lapse sequence of R1 spindles confined within a microfabricated channel.

**Fig. 3. R1 spindles elongate by insertion of ParM monomers at the ParR/*parC* complex.**

(A) Photobleaching (indicated by red arrows) of ParM spindles reveals symmetrical, bipolar elongation at the bead surface.

(B) ParM spindles elongate at each end at the same rate as free filament ends. The distance between the two photobleached stripes or distance between the stripe and the bead in (A) was measured on a per-frame basis, and the change in distance was plotted against time.

(C) By speckle microscopy all new ParM monomers add to the spindle at the ParR/*parC* interface. Green: Alexa-488 ParM. Red: rhodamine-ParM doped at 1:1000 to produce fluorescent speckles. Left: time-lapse sequence of an elongating spindle end (80 seconds/frame). Right: kymograph of the time-lapse sequence.

**Fig. 4. Dynamic instability of free ParM filaments provide the energy for R1 spindle elongation**

(A) The ParR/*parC* complex stabilizes ParM filaments down to the ParM-ATP critical concentration. Spindle assembly reactions were performed at the indicated concentrations of Alexa-488-labeled ParM.

(B) By abolishing the difference in critical concentration between free and ParR/*parC* bound ParM filaments, AMPPNP eliminates sustained polymerization on ParR/*parC* - beads.

(C) Small amounts of ATP added into AMPPNP restores sustained polymerization on ParR/*parC* beads.

(D) Hydrolysis-dependent ParM tail elongation occurs specifically at filament ends bound to ParR/*parC* complexes and not at free filament ends. Assembly reactions as in (C) were initiated with Alexa-488 ParM (green), at indicated times the reactions were



spiked with cy3-ParM (red). Results were visualized after 50 minutes. 2 examples of each time point are shown.

(E) Rates of ParM tail elongation scale with the fraction of hydrolysable nucleotide.

Reactions as in (C) were performed at various ATP:AMPPNP ratios. The rate of tail elongation was plotted against the percent of ATP within the nucleotide mixture.

## Supporting Text

### Conditions for experiments shown in each figure.

Figure 1A,B. 0.3 $\mu$ m ParC-*cy3* coated beads, 5 $\mu$ M ParM doped containing 30%-Alexa-488 labeled ParM, 300nM ParR, and 10mM ATP.

Figure 1C. Same as 1A, but with 3mM AMPPNP and 7mM ATP as the nucleotide.

Figure 1D. Same as 1A.

Figure 1E. Same as 1A, save 2.6 $\mu$ M unlabeled ParM for the 2 left-most images, and 5 $\mu$ M unlabeled ParM for the 2 images in the right column.

Figures 1(F-G). Same as 1A.

Figures 2(A-C). Same as 1A.

Figure 3A. Same as 1A.

Figure 3C. 7 $\mu$ M 30% Alexa-488 labeled ParM doped with 7nM Rhodamine ParM, 300nM ParR 0.3 $\mu$ m *parC* coated beads (with no *cy3* moiety), and 10mM ATP.

Figure 4A. All concentrations are the same as in 1A, save 30%-Alexa-488 labeled ParM was used at the indicated concentrations.

Figure 4B. 3 $\mu$ m *parC-*cy3** coated beads, 5 $\mu$ M ParM 30% Alexa-488 ParM, and 300nM ParR were combined with 10mM AMPPNP.

Figure 4C. Same conditions as 4B, save the reaction was polymerized with 9.5 mM AMPPNP and 0.5mM ATP.

Figure 4D. 3 $\mu$ m *parC* coated beads (with no *cy3* moiety), 300nM ParR and 5.6 $\mu$ M 30% Alexa-488 labeled ParM were combined with 7.5mM ATP

and 92.5mM AMPPNP. At the indicated time points an equal volume (to the initial reaction volume) of an identical solution with no beads) containing of 5.6 $\mu$ M 30% cy3 labeled ParM was added.

Figure 4E. Same conditions as 4B, save the reaction was polymerized with 10mM nucleotide total containing the indicated fraction of ATP.

**ParR/*parC* does not change the critical concentration of bulk ParM solutions.**

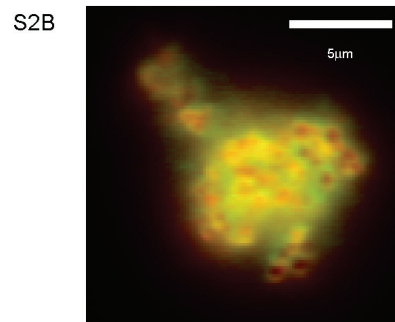
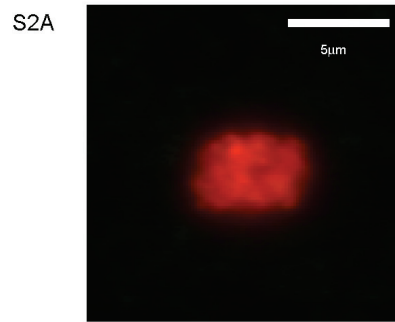
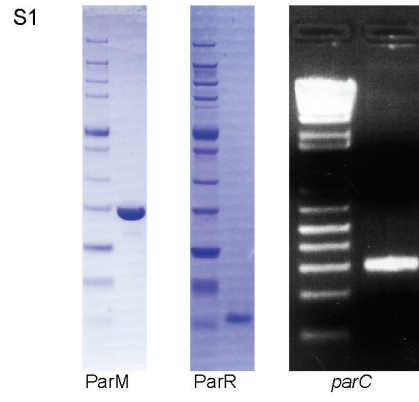
Previous work utilizing light scattering assays (S8) suggested that ParR/*parC* could facilitate polymerization of bulk solutions of ParM beneath the steady state ATP critical concentration of 2.3 $\mu$ M. Despite repeated efforts, we have been unable to replicate this result using either light scattering or FRET polymerization assays. Shown in Figure S7 is one such experiment, where the FRET polymerization signal is unchanged by the addition of ParR/*parC*. As the FRET polymerization signal is proportional to the total amount of polymer (S1), one would expect the ParR/*parC* complex, if it were lowering the critical concentration of the solution, to cause an increase in the total polymer and hence increase the total FRET signal. In our hands, even high concentrations of ParR/*parC* do not increase the amount of polymer in solution; hence we conclude that the ParR/*parC* complex does not change the critical concentration of bulk solutions of ParM.

This result is not at odds with our observation that the ParR/*parC* complex can stabilize bipolar bound filaments within the spindle down to the ATP ParM critical concentration. This is due to the fact that in order for an end-binding factor to shift the critical concentration of filaments within a solution, that factor needs to be saturating in respect

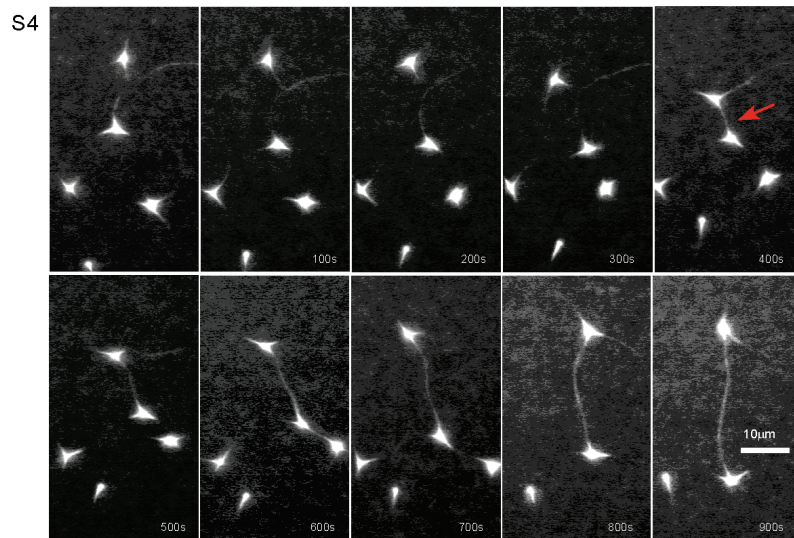
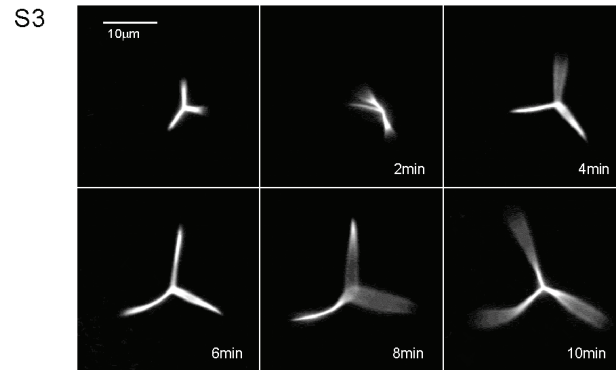
to the filament ends. We note that the concentration of bead coupled *parC* DNA within our spindle reactions is much less than the high concentrations of free DNA (40nm) utilized within our FRET experiments, concentrations that are not saturating enough to shift the critical concentration. Hence we conclude that in our assays, as well as within the bacterium, the critical concentration of the ParM bulk solution is unchanged due to the low abundance of *parC* molecules, as *parC* is not saturating in respect to ParM filament ends.

- S1. E. C. Garner, C. S. Campbell, R. D. Mullins, *Science* **306**, 1021 (Nov 5, 2004).
- S2. D. Popp *et al.*, *Biochem Biophys Res Commun* **353**, 109 (Feb 2, 2007).
- S3. J. C. McDonald, G. M. Whitesides, *Acc Chem Res* **35**, 491 (Jul, 2002).
- S4. Y. W. Xia, G. M., *Angewandte Chemie International Edition* **37**, 550 (1998).
- S5. D. C. M. Duffy, J. C.; Schueller, O. J. A.; Whitesides, G. M., *Anal. Chem.* **70**, 4974 (1998).
- S6. V. Girish, A. Vijayalakshmi, *Indian J Cancer* **41**, 47 (Jan-Mar, 2004).
- S7. U. E. R. P. Thévenaz, M. Unser, *IEEE Transactions on Image Processing* **7**, 27 (1998).
- S8. J. Moller-Jensen, R. B. Jensen, J. Lowe, K. Gerdes, *Embo J* **21**, 3119 (Jun 17, 2002).

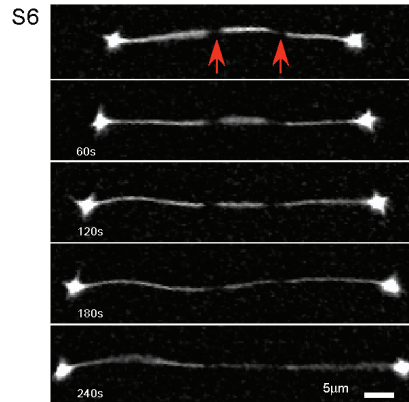
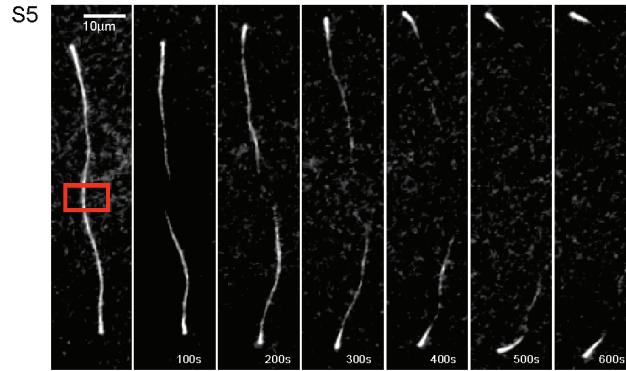
## Supplementary Figures



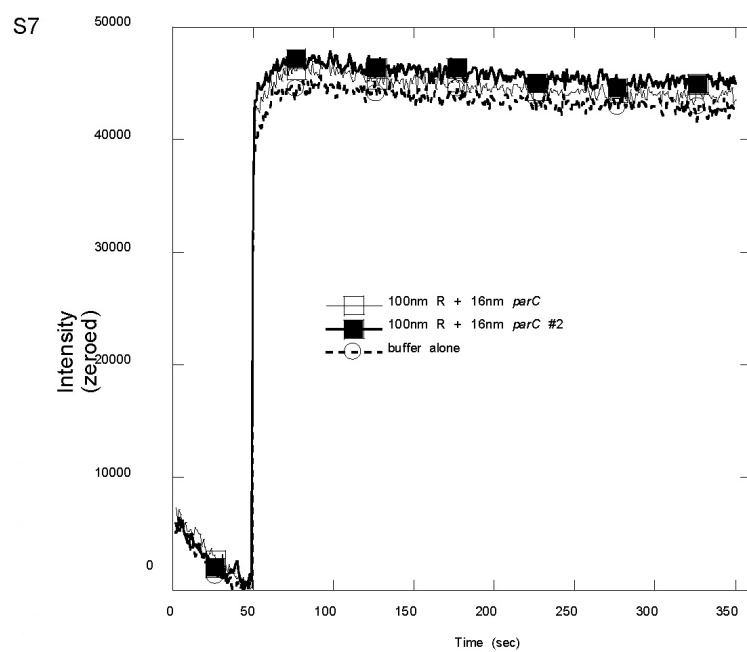
Supplementary Figures (cont.)



Supplementary Figures (cont.)



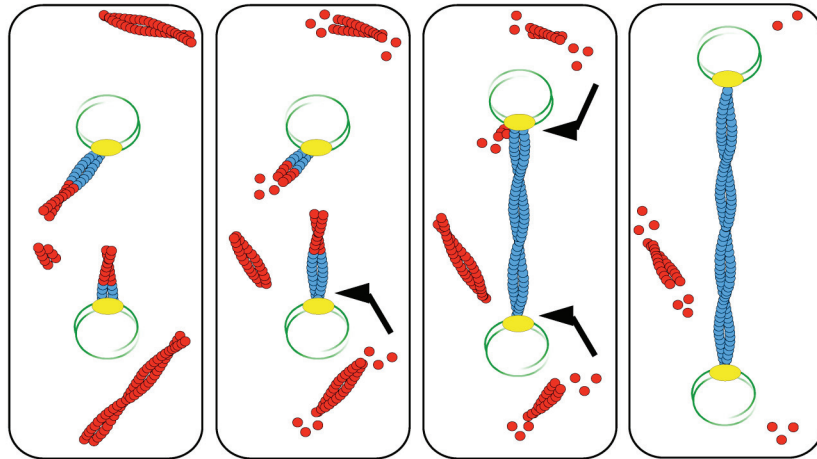
Supplementary Figures (cont.)





Supplementary Figures (cont.)

S8



## Supplementary Figure Legends

### **Figure S1A – Purified components used in all experiments.**

Comassie stained SDS-PAGE gels of purified ParR and purified ParM. Shown also is an ethidium bromide stained agarose gel of double stranded DNA containing the *parC* sequence.

### **Figure S2A - Image of the same reaction as in Figure 1A, but without the addition of ParR.**

### **Figure S2B - Image of the same reaction as Figure 1A, but with nonspecific cy3-labeled DNA conjugated to the beads.**

### **Figure S3 - Time lapse series of a stabilized ParM star elongating under stabilizing conditions, as in Figure 1C.**

Shown only is the Alexa-488 channel.

### **Figure S4 - Another example of search-and-capture formation of R1 spindles.**

Conditions are identical to 2A.

### **Figure S5 - Another example of severing bipolar ParM spindles with laser irradiation.**

Red box indicates the region photobleached. Conditions are identical to 2B.

**Figure S6 - Another example of bipolar elongation as measured by marking the spindle with photobleaching.**

Red arrows indicate points of photobleaching at time zero. Conditions are identical to 3A.

**Figure S7 – Free ParR/*parC* does not change the steady state critical concentration of ATP-ParM.**

14 $\mu$ M ParM containing 20% Cy3 and 20% Cy5 labeled monomer was combined with 200nm ParR and either 40nm *parC* or buffer. At 10 seconds the solution was induced by the addition of 5mM ATP.

**Figure S8 - Model for R1 segregation.**

The ParR/ *parC* complex can capture ParM filaments that nucleate randomly throughout the cytoplasm. Filament ends that are bound by ParR/*parC* are stabilized against catastrophe (blue) while unbound filaments are unstable (red) and destined to undergo catastrophe. Filaments that are bound and stabilized at one end by a single plasmid can then search for the opposing plasmid. Only when both filament ends are bound by ParR/*parC* is the entire spindle stabilized. Turnover of the unbound, background filaments then provide the energy differential (arrows) that powers the elongation and long-axis detection of the R1 spindle.

## Supplementary Movies

All movies are available online at

<http://www.sciencemag.org/cgi/content/full/sci;315/5816/1270/DC1>

### **Movie S1 – Movie of a single bead with ParM asters emanating out of the bead.**

Imaged is the Alexa-488 ParM channel. Scale bar is 2 microns. Frames are 5 seconds apart.

### **Movie S2 – Movie of stabilized asters growing out of a single bead.**

Imaged is the Alexa-488 ParM channel. Scale bar is 5 microns. Frames are 2 minutes apart.

### **Movie S3 – Movie of R1 spindles elongating over long distances.**

Imaged is the Alexa-488 ParM channel. Scale bar is 10 microns. Frames are 20 seconds apart.

### **Movie S4 – 2 color movie of R1 spindles.**

Green is Alexa-488 ParM channel, and red is the *cy3-parC* channel. Scale bar is 10 microns. Frames are 20 seconds apart.

### **Movie S5, S6 – Movies of multipolar R1 spindle elongation.**

Imaged is the Alexa-488 channel. Scale bar is 10 microns. Frames are 20 seconds apart.

**Movies S7, S8 – Movies of search and capture events between *parC* coated beads.**

Imaged is the Alexa-488 channel. Scale bar are 5 microns. Frames are 20 seconds apart.

**Movie S9, S10 – Movies of photosevering of ParM spindles.**

Imaged is the Alexa-488 channel. Scale bars are 10 microns. Frames are 10 seconds apart.

**Movie S11 – Combined movies of R1 spindles elongating within PDMS molds.**

Frames are 20 seconds apart.

**Movie S12 – Movies of spindle elongation in respect to photobleached marks.**

Imaged is the Alexa-488 channel. Scale bar is 10 microns. Frames are 10 seconds apart.

**Movie S13, S14 - Movies of Alexa-488 labeled R1 spindles speckled with TMR-ParM.**

Imaged is the Alexa-488 channel (green) and the TMR channel (red). Scale bars are M13 are 2.5 microns. Frames are 20 seconds apart.

**Movie S15, S16 – Movies of monopolar, stabilized ParM tails pushing 3 micron beads.**

Reactions were polymerized with 100mM nucleotide total (95% AMPPNP and 5% ATP).

Imaged is the Alexa-488 channel. Scale bars are 5 microns. Frames are 1 minute apart.

**Movie S17 – Animated model of R1 plasmid segregation.**

## **Materials and Methods**

### **ParR purification:**

ParR was PCR amplified from the R1-19 plasmid, ligated into a pet-11a vector and sequenced. BL21 cells were transformed with this construct, grown to an OD 600 of 1.0 and induced with 0.5mM IPTG for 4 hours. Cells were spun down and resuspended in a buffer containing 50mM MES pH 6.0, 100mM KCL, 2mM EDTA, 5% glycerol, 2mM DTT, and a small amount of DNase and lysozyme. Cells were briefly sonicated, then lysed by three passages through a microfluidizer. The cell lysate was subjected to two ammonium sulfate cuts, 0-25% and 25-50%. The 25-50% ammonium sulfate cut was resuspended in Buffer 1 (25mM MES pH 6.0, 1mM DTT, and 1mM EDTA). This was then diluted in the same buffer to a final volume of 150mls and then rapidly loaded onto a 5-ml HiTrap S column. Bound proteins were and eluted with a gradient of 0-1M NaCl in the background of the Buffer 1. Peak fractions were collected and concentrated to 0.5mls in a YM-10 centricon. This was then dialyzed into buffer R (300mM KCL, 30mM MES pH 6.0, 1mM EDTA, 1mM DTT) and subsequently gel filtered over an S200 column equilibrated in Buffer R. Pure fractions were then pooled, and frozen in 20% glycerol. The sample was verified to be ParR with MALDI mass spectroscopy. Concentration was determined with quantitative SDS\_PAGE densitometry using the stain SYPRO-Red.

### **Expression and purification of ParM:**

DNA encoding ParM was PCR-amplified from the R1-19 plasmid using primers that, when translated, add five additional amino acids (GSKCK) to the C-terminus. The KCK

sequence was appended to enable covalent attachment of fluorescent probes containing sulfhydryl-reactive functional groups. The PCR product was cloned into a pet-11a vector and sequenced. BL21 cells were transformed, grown at 37°C to an OD600 of 1.0, and induced with 1mM IPTG for 4 hours. Protein was purified as described (SI), dialyzed into Buffer F (100mM KCl, 30mM Tris HCl pH 7.5, 1mM DTT, 2mM MgCl<sub>2</sub>), and gel filtered over a Superdex 75 column equilibrated in Buffer F. Peak fractions were frozen in 20% glycerol.

#### **Creation of a biotinylated *parC*:**

*ParC* was amplified from the R1-19 plasmid using primers that would yield an *nde1* cut site 5' to the sequence repeats and a 3' *bamH1* site. This was ligated into a pet11a vector and sequenced. Primers were then designed from this plasmid that would generate a 356bp stretch of DNA containing the *parC* sequence. Primers were created such that we could PCR stretches of DNA that could contain or lack a 5'-biotin and/or a 3'-cy3 moiety.

#### **Labeling of ParM with fluorescent dyes:**

Glycerol and DTT were removed by a PD10 salt exchange column equilibrated in Buffer F without DTT. For labeling we added a 5-fold molar excess of dye to protein and incubated for 10 minutes at 25°C. We quenched the reaction with 10mM DTT and removed free dye by gel filtration on G25 resin. Samples were frozen down following addition of 0.2M sucrose. Average labeling efficiency for samples used in this study was 100±15%.

**DNA-Bead coupling:**

50  $\mu$ L of spherical streptavidin coupled magnetic beads (Bangs labs) were washed with 1.5ml wash buffer (10mM Tris HCl pH 8.2, 1M NaCl, 1mM EDTA) three times using a magnetic separator. Beads were then resuspended in 1.3mL wash buffer + 0.2% Tween 20. 200uL of biotinylated DNA (ranging 200uM-400uM) was added to the tube, mixed, and incubated for 1 hour. The beads were then washed three times with 1.5mL wash buffer, followed by washing twice with 1.5mL buffer FE (30mM Tris HCl pH 7.0, 100mM KCL, 1mM EDTA). Beads were resuspended in 50uL FE and stored on ice.

**Slide preparation:**

We find that when doing microscopy on ParM filaments and ParM spindles, careful consideration of the surface chemistry issues of glass is paramount. Clean glass (glass that has been acid washed or base washed) is sufficiently sticky to adsorb monomers onto its surface, denaturing ParM over time. When a small amount of sticking to glass is desired, for instance in a TIRF assay, cleaned glass can be used to promote transient adsorption, but only when there is adequate protein blocking reagents such as BSA or casein included in the solution to limit the glass adsorption. As with any protein, failure to include blocking reagents leads to nonspecific sticking onto the slide and protein denaturation. In our experience, inadequate blocking leads to the formation of non-dynamic, needle-like bundled structures of dead protein. These aggregates are also observed near air bubbles and slides left out overnight. Structures such as these were observed by Popp, D. et. al (S2), who used hydrofluoric acid washed glass with no



protein blocking reagents within their assays. When developing the spindle assay, we tested many different protein blocking conditions. This led us to realize that protein blocking yields inconsistent slide coating across the field as well as from slide to slide, conditions that are unacceptable for long time courses. Given the inhomogeneity produced by blocking the glass with proteins, we have turned to chemical derivitization, where we treat slides in such a manner so that protein adsorption onto the glass surface of slides is almost eliminated.

To accomplish this, all of the optical glass used in these experiments was covalently derivitized with diethyl-dichloro silane. Slides and coverslips were cleaned by sonicating in ethanol, washing extensively with ddH<sub>2</sub>O, sonicating in 0.1M KOH, washing extensively with H<sub>2</sub>O, and finally sonicating in ethanol. Slides were washed in silanization solution (95% isopropanol, 5% H<sub>2</sub>O, pH 5.) then silanized by sonicating in a 2% solution of diethyl-dichloro silane in silanization solution. Slides were then washed and subsequently sonicated in silanization solution, and dried overnight in a drying oven. Slides were then washed with ethanol, then sonicated in ethanol, slowly dipped into ddH<sub>2</sub>O, and dried overnight.

**R1 spindle assembly:**

DNA coated beads were combined with 30% Alexa-488 labeled ParM, 300nM ParR, 0.4% methylcellulose (400 centipoise), and 15mg/ml BSA (to minimize slide adsorption). The reaction was spotted on the slide and polymerized with 1/10<sup>th</sup> of the solution volume of 100mM ATP. Reactions were covered with a coverslip and sealed with valap to avoid

oxidation. Microscopy was performed on an inverted epifluorescence microscope (TE300, Nikon) fitted with a cooled CCD camera (OrcaII, Hamamatsu).

### **Electron microscopy of R1 spindles:**

Bead samples were prepared as described above without the addition of BSA. After polymerization, 10uL of sample was applied to glow-discharged, carbon-coated grids. The grids were then stained with 2% aqueous uranyl acetate and rinsed twice by dipping in water. After drying, the grids were visualized on a Tecnai T20 electron microscope at 200kV.

**Dual color polymerization assay:** *ParC* containing DNA was PCR amplified from the *parC* pet vector using primers that added a 5' biotin group and no 3' fluorescent label. This was conjugated to 2.93uM spherical magnetic beads (as above). Beads were combined into a solution of 280nM ParR, 0.2% methyl cellulose, 15mg/ml BSA, and 5.6uM 30% Alexa-488-labeled ParM. An identical solution was made that contained 5.6uM 30% cy3-labeled ParM but contained no *parC* beads. 5uL of the Alexa-488 labeled reaction was polymerized by the addition of 1uL of 7.5mM ATP and 92.5mM AMPPNP. After the indicated amount of time, 5uL of the cy3-labeled reaction was added to the tube and gently mixed. All reactions were gently spotted onto slides and visualized at 50 minutes.

### **Photobleaching experiments:**

Spindle assembly reactions were prepared as above, with the only difference being a smaller volume being spotted (0.5-1uL) on the slide to assist in keeping the entire spindle within the plane of focus. Spindles were visualized with a LSM510 confocal microscope (Zeiss). After waiting ~10 minutes for the bundles to elongate, spindles were photobleached with transverse stripes 2 pixels thick, with 200 iterations of photobleaching for spindle marking experiments, and boxes ~10 pixels thick with 1000 iterations of photobleaching for severing experiments.

### **Speckling experiments:**

Spindle assembly reactions were prepared as in the R1 spindle assays, with the addition of Rhodamine ParM at a ratio of 1:1000 to total ParM. 100mM mercaptoethanol was also added into the reaction to reduce photobleaching. Spindles were visualized with a LSM510 confocal microscope (Zeiss).

### **Fabrication of Microchambers:**

Microchambers were fabricated out of the polymer poly(dimethylsiloxane) (PDMS) using the techniques of soft lithography and rapid prototyping(S3-S5). The four designs consisted of arrays of microchambers with the following dimensions: i) 1.6  $\mu\text{m}$  wide, 15  $\mu\text{m}$  long, 1.5  $\mu\text{m}$  tall; ii) 1.6  $\mu\text{m}$  wide, 10  $\mu\text{m}$  long, 1.5  $\mu\text{m}$  tall; iii) 2  $\mu\text{m}$  wide, 15  $\mu\text{m}$  long, 1.5  $\mu\text{m}$  tall; iv) 2  $\mu\text{m}$  wide, 10  $\mu\text{m}$  long, 1.5  $\mu\text{m}$  tall. Microfabricated masters consisting of photoresist (Shipley) patterned on silicon wafers were prepared using UV lithography through a transparency mask designed on a computer using a CAD tool. We silanized the masters with a vapor of tridecafluoro-1,1,2,2-tetrahydrooctyl trichlorosilane,

poured PDMS prepolymer (Sylgard 184) on the masters, and cured the elastomer thermally. The slab of PDMS with microchambers embossed on the surface was cut out with a scalpel and peeled away from the master.

### **Visualization of R1 spindle dynamics in Microchambers:**

Spindle assembly reactions were prepared as above, and 4.5 $\mu$ L spotted onto a strip of parafilm. These were polymerized by addition of 0.5 $\mu$ L 100mM ATP. 1 $\mu$ L of this reaction was spotted onto a 24 x 50 mm coverslip (silanized as above). PDMS molds were then placed onto the coverslip with the chambers facing the coverslip, and pressed firmly to create a seal between the slide and the coverslip. The field was scanned to locate regions that had a tight seal with the sample trapped within the microchambers. Microscopy was performed on an inverted epifluorescence microscope (TE300, Nikon) fitted with a cooled CCD camera (OrcaII, Hammamatsu).

### **Image Processing:**

All movies were processed using NIH ImageJ (S6). Any brightness or contrast adjustments were applied to the entire image field and stack uniformly. When there was fluid flow within the samples, the images of beads and spindles were centered throughout the stack by using the Stackreg ImageJ plugin (S7).

**Chapter 5**  
**Unpublished Experiments.**

## **Introduction**

The intention of this chapter is to include the useful morsels of experimental results, details, and general ParM bizarreness that never made it into any publications. While many of these details are not critical for understanding the overall function of the R1 spindle, these experiments explain a lot of the minutiae of the polymerization kinetics and dynamics of ParM, especially when utilizing nucleotide analogs. I have spent some time cataloging these results for any that come after me, to help minimize any confusion they may encounter.

## **Polymerization conditions of ParM**

Upon starting this work, I wished to find buffer conditions under which ParM would not polymerize. Eukaryotic actin does not polymerize at low salt or high pH, and polymerization is more favorable in  $Mg^{2+}$  over  $Ca^{2+}$ . As such, polymerization is induced by the addition of KMEI to the protein solution, causing a simultaneous increase in the salt, a decrease in pH, and swapping out of the free  $Ca^{2+}$  in the solution for  $Mg^{2+}$ . As these conditions are useful for the study of eukaryotic actins, I wished to attempt to determine similar salt and pH conditions for ParM. As seen in Figure 1A, ParM polymerizes at a range of salt concentrations, with only a modest decrease in polymerization at zero salt. ParM also appears to be fairly pH insensitive, as polymerization is similar across the range of 5-9 (figure 1B). At pH 4, the protein simply denatured, as white precipitate formed at the bottom of the tube. As ParM can polymerize

across a range of salt and pH conditions, but that the apo or ADP form does not polymerize, we utilized the presence of ATP as the basis for controlling polymerization.

We also tested the nucleotide specificity for ParM polymerization. ParM can polymerize with a number of nucleotide tri-phosphate analogs. As seen in Figure 1C, ParM can polymerize with ATP, AMPPNP, ATP- $\gamma$ -S, GTP, and GCPPCP. Polymerization does not occur with GTP- $\gamma$ -S. however.

### **The nucleotide state affects the nucleation rate of ParM filaments.**

Shown in figure 2A-E are a series of traces showing ParM polymerization in various nucleotide analogs. Shown also is a series of traces showing polymerization of the hydrolysis dead mutant. Careful examination of these traces yields 2 important findings. First, if one compares the polymerization traces of the “trapped” ATP forms of ParM (AMPPNP, ATP- $\gamma$ -S, or E148A, Figures 2B,D,E) to form of ParM that can hydrolyze ATP (ATP, ATP-BeF<sub>3</sub>, Figures 2A,C), the nucleation rate appears to be much slower. This same trend appears to hold for GTP and its non-hydrolysable analogs (Figure 1C).

Aside from the nucleation rate being much slower, in these hydrolysis deficient conditions the nucleation rate also appears to scale differently than that wild type ATP-ParM. Nucleation scaling of the E148A mutant shows a slope of 3.5 (figure 3A), a value much higher than that of (1.5) ParM or actin (see chapter 4 figure 2A).

We were able to verify that these hydrolysis dead conditions were indeed nucleation limited by demonstrating that preformed seeds could overcome the nucleation barrier. Figure 3B demonstrates that EGS crosslinked filaments, when added to a reaction of polymerizing E148A-ParM, can accelerate the polymerization reaction in a titratable manner. Other experiments also demonstrated that by simply adding pre-polymerized AMPPNP filaments to a polymerizing reaction of AMPPNP ParM could also hasten the polymerization reaction (data not shown).

An outstanding question is how the polymerization of ATP-ParM is able to generate so many nuclei so quickly. It appears that the hydrolysis of ATP hastens the nucleation, as the nucleation rate of  $\text{BeF}_3$ -ATP-ParM appears identical to ATP-ParM (Figure 3C). Similarly, if a slowly nucleating reaction of AMPPNP ParM is doped with small amounts of ATP, the reaction polymerizes much faster (Figure 3D). In fact, the initial velocity of the polymerization of an ATP-doped reaction appears to occur at the same rate as a reaction polymerized with ATP alone (figure 3E), suggesting that the nucleation by ATP ParM is dominating these reactions.

While an explanation for this data is by no means obvious, it may be that the ATP ParM within these reactions is providing fragility to the filaments, such that filaments can break and contribute extra ends into the reaction. This breakage could also be hastened by the rapid pipetting of ATP into a cuvette, or the shear forces the solution is subject to when it is combined with ATP in a rapid mixer.



One final point to note is that the polymerization traces that result when polymerizing ParM with ATP- $\gamma$ -S are very sporadic and irreproducible (see Figure 2D), with nucleation rates ranging wildly from experiment to experiment. It is for this reason we have shied away from using ATP- $\gamma$ -S for any kinetic experiments, and rather utilized AMPPNP.

### **The nucleotide state effects the FRET polymerization signal.**

The second surprising result from the FRET polymerization data is that the FRET signal for the ATP trapped form is much higher than the hydrolysis capable form of the protein. This is demonstrated by figure 2F, where the same concentration of ParM is polymerized in various nucleotides. Another notable result that adding ADP to ParM yields an even lower signal than buffer alone. These results suggest that the nucleotide state of the monomers within the filament affect the overall FRET assay polymerization signal. While one would expect there to be a higher polymerization signal due to the increase in total polymer, in all cases the plateau values were far higher than the signal increase expected for the 1.7 $\mu$ M more ParM being in a polymerized state.

To verify that the FRET signal was polymerization was indeed linear in respect to concentration for each nucleotide analog, I polymerized ParM at a range of concentrations with the nucleotides ATP, AMPPNP, and ATP- $\gamma$ -S. This experiment is shown in Figure 4A, with only a subset of the data shown for clarity. If one then plots the florescence increase vs. concentration (Figure 4B) an interesting trend emerges. While all three series are linear in respect to concentration, the slope of the line is much greater for AMPPNP and ATP- $\gamma$ -S. In fact, these two analogs show a similar slope,

suggesting that the common hydrolysis state they cause within the protein is causing an identical increase in the fluorescent signal. These increases in fluorescence are reproducible from sample to sample, even with nucleotide mixtures. Figure 4C shows that sequential additions of nucleotide can result in similar final plateau values, even when added in different order.

The origin of this nucleotide dependent increase in fluorescence is puzzling. This increase in fluorescence is seen in all cases of the hydrolysis dead forms of ParM, being in polymerization with AMPPNP, ATP- $\gamma$ -S, GTP- $\gamma$ -S, and E148A. This increase is also observed when ParM is polymerized in ATP with the phosphate analog BeF<sub>3</sub> (Figure 2C), suggesting that this fluorescence increase may also be present in the ADP-Pi state as well as the ATP state of the filament.

This effect may not be dependent only on the hydrolysis state of individual monomers, as it may be that the conformation (or twist) of the filament effects the FRET signal, and that the filament twist (or breathing modes) are effected by the nucleotide state of the local monomers in that region. Evidence for this idea is present in doping experiments, where small amounts of E148A ParM shift the fluorescence of wild type ParM (Figure 4D) up to the E148A fluorescence level. These curves are identical to the E148A stabilization curves shown in Chapter 3 Figure 3C, suggesting that this fluorescence increase scales with the change in the critical concentration observed in the pelleting experiments. If the fluorescence increase truly is a readout of filament conformation, these results have important implications. This would suggest that, like actin, the breathing modes of ParM

filaments are nucleotide dependent and that changes in the hydrolysis state of a monomer can propagate through the filament structure. Furthermore, the simultaneous change in the FRET signal and the critical concentration implies that the breathing modes of the filaments and long range allosteric effects do indeed influence both the critical concentration as well as filament dynamics.

### **ADP Poisoning effects on ParM polymerization and nucleation.**

The presence of ADP is inhibitory to ParM polymerization. Solutions of ParM polymerized in ATP will be depolymerized when the total nucleotide consists of 20% ADP (Chapter 3 figure 2D). Furthermore, spontaneous polymerization of ParM will not occur when the added nucleotide contains more than 20% ADP. The ADP poisoning effect comes from accelerating the off rate of monomers from the ends of filaments, as solutions of polymerized ParM will depolymerize two fold faster when diluted into ADP over buffer alone (chapter 3 supplemental figures 3C-D). We believe the acceleration of depolymerization occurs through nucleotide exchange at the ends of filaments, as nucleotide exchange does not occur within the filament (RDM, unpublished data).

This ADP poisoning effect can be seen in a very pronounced manner when looking at the nucleation limited AMPPNP polymerized filaments. Increasing amounts of ADP will slow down the rate of polymerization trace in a titratable manner. (Figure 5A) This reaction appears to be nucleation limited, as ATP or preformed filaments can completely eliminate this lag. Our interpretation of these results is that the slowly appearing nuclei

formed in AMPPNP are destabilized by ADP, so that elongation off of spontaneous nuclei is in competition with depolymerization induced by ADP.

Despite numerous attempts, I have been unable to see any of the reported effects of the ParR/*parC* complex on the critical concentration ( $I$ ) or nucleation rate of ATP ParM. However, the nucleation limited destabilized conditions provide an interesting testbed to examine the effect of the ParR/*parC* complex on polymerization. Under destabilizing conditions, I find that the ParR/*parC* complex accelerates the polymerization of ParM in a titratable manner (Figure 5B). This acceleration of polymerization can come from two sources; 1) either the ParR/*parC* complex is nucleating ParM filaments, or 2) the ParR/*parC* complex is stabilizing the spontaneous nuclei against ADP destabilization. From this data alone it is difficult to differentiate between these two possibilities. In Chapter 4, we demonstrate that the ParR/*parC* complex stabilizes ADP filaments down to the ATP critical concentration, suggesting that the ParR/*parC* complex can cause ADP ends to act as to ATP ends. This leads us to favor the possibility that the acceleration of nucleation in the nucleation-limited destabilized system is coming from the ability of the ParR/*parC* complex to protect the nuclei against ADP mediated depolymerization.

### **Characterization of Monopolar ParM tails.**

Previous to the bipolar stabilization of ParM tails discussed in chapter 4, I spent a great deal of time (~1 year) elucidating the monopolar, stabilized tails shown in Chapter 4 figure 4C. The reason the bipolar stabilization was not observed sooner was due to the fact that

bipolar connections cannot form between beads that are 3 $\mu$ m in size, but do form between beads 0.3 $\mu$ m in size. (Figure 6A).

When studying these monopolar tails, a few things were noted. First these tails appeared to be hollow, as confocal sections through the tail yielded a minimum of intensity in the center of the tail (Figure 6B). Polarization microscopy indicated that these tails are composed of linear filaments aligned along the direction of motion (figure 6C). These results are interesting in light of actin literature, as actin tails propelling ActA mediated beads are highly crosslinked arrays with no hollow core. However, if conditions are altered in such a manner so that elongation is favored over ARP2/3 mediated nucleation, the tails also become hollow. This has been accomplished either through depletion of ARP2/3 and the addition of fascin (2), and also through the VASP mediated acceleration of filament elongation (3).

The final, unpublished result is that when these monopolar tails are directed to push against oil droplets coated with *parC*, these tails do not exert any squeezing forces on the oil droplet (figure 6D). This demonstrates, not surprisingly, that this motility cannot be explained through an elastic gel model (4) and rather is more likely explained through insertional polymerization at the bead surface.

1. J. Moller-Jensen, R. Jensen, J. Lowe, K. Gerdes, *Embo J* 21, 3119 (2002).
2. W. Brieher, M. Coughlin, T. Mitchison, *The Journal of cell biology* 165, 233 (May, 2004).

3. J. Plastino, S. Olivier, C. Sykes, *Current biology: CB* 14, 1766 (Oct, 2004).
4. J. van der Gucht, E. Paluch, J. Plastino, C. Sykes, *Proceedings of the National Academy of Sciences of the United States of America* 102, 7847 (May, 2005).

Figure 1

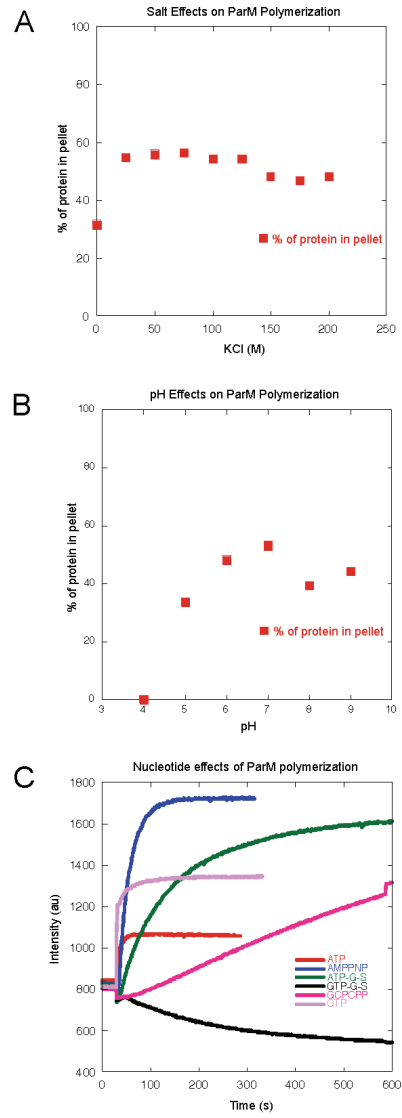


Figure 2

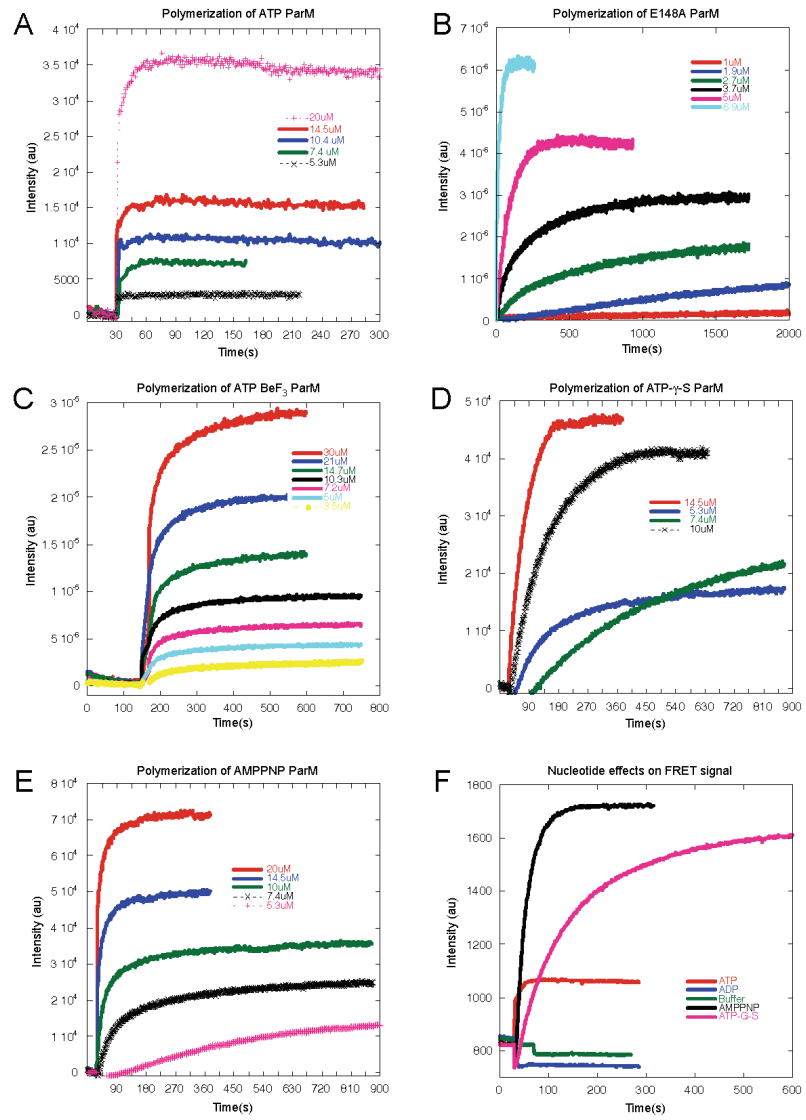




Figure 3

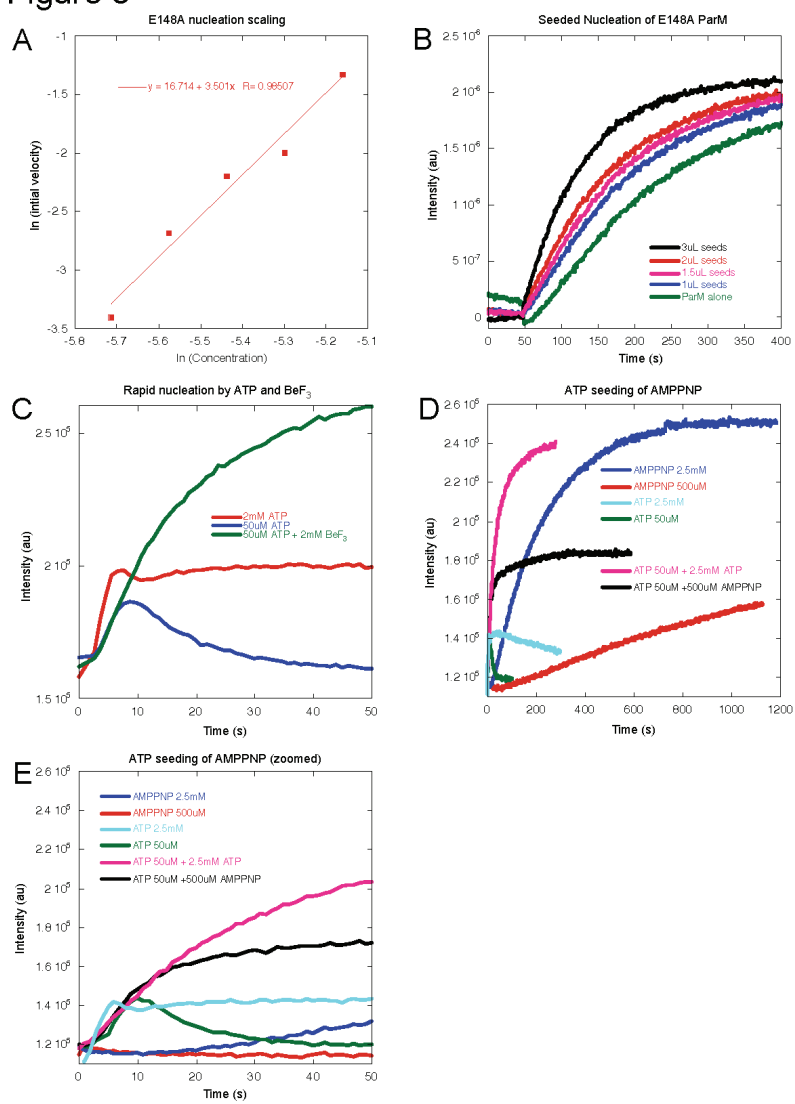


Figure 4

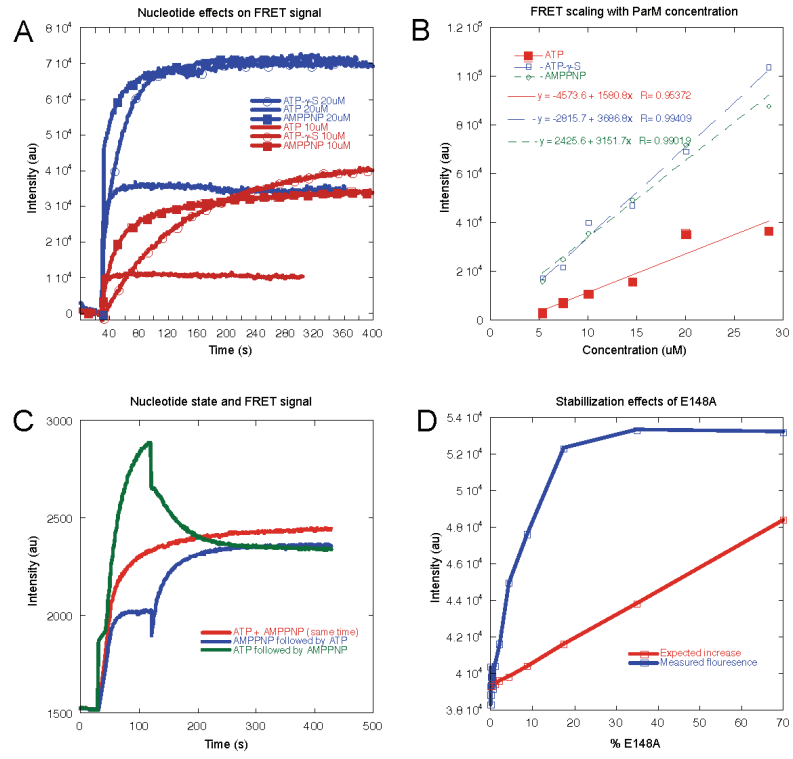


Figure 5

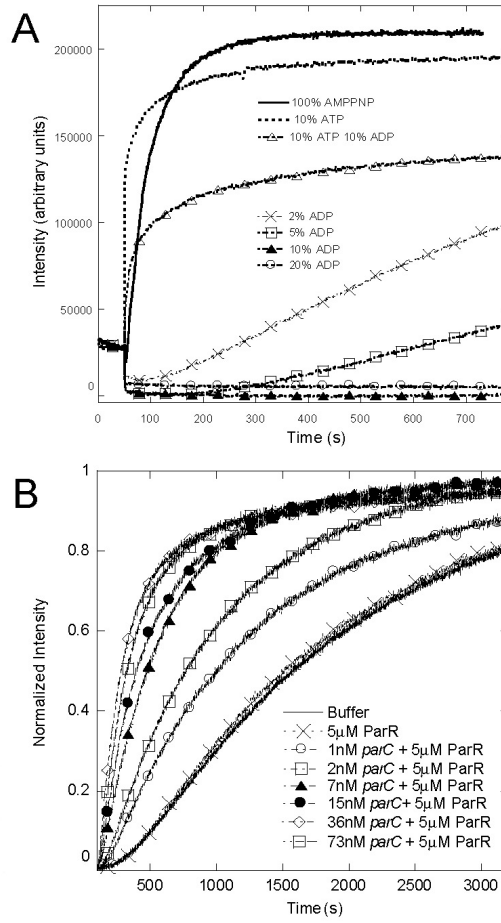
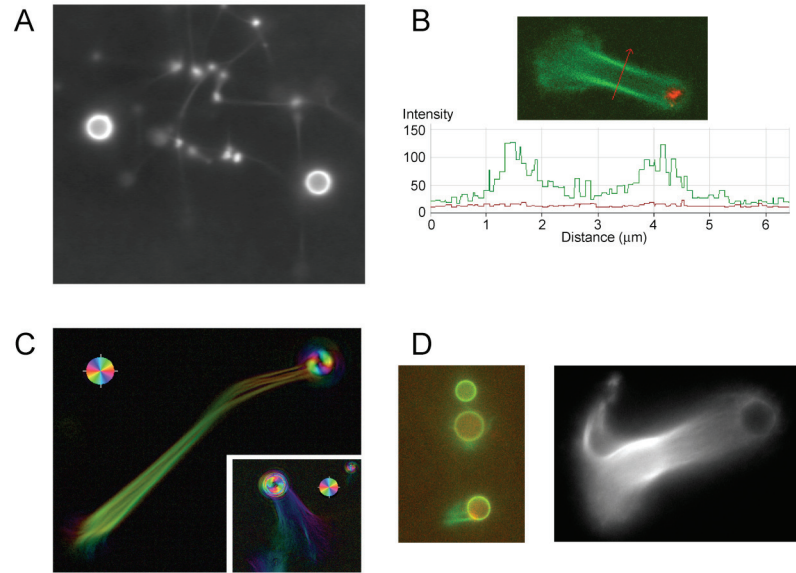


Figure 6



## Figure legends.

### Figure 1.

#### A) pH dependence of ParM polymerization.

12uM of ParM was induced to polymerize by addition of ATP. Buffers were identical to buffer F, save buffering components were utilized to adjust the solution to the indicated pH. After 20 minutes of incubation, the samples were spun for 15 minutes in a TLA 100.4 at 100,000 rpm. Pellet and supernatant were separated, and the pellet fraction was resuspended in a constant volume, run on an SDS-Page gel, quantified with NIH ImageJ, and plotted.

#### B) Salt dependence of ParM polymerization.

12uM of ParM was induced to polymerize by addition of ATP. Buffers were identical to buffer F, save KCl content was utilized to adjusted as indicated. After 20 minutes of incubation, the samples were spun for 15 minutes in a TLA 100.4 at 100,000 rpm. Pellet and supernatant were separated, and the pellet fraction was resuspended in a constant volume, run on an SDS-Page gel, quantified with NIH ImageJ, and plotted.

#### C) Nucleotide dependence of ParM polymerization.

12uM of FRET labeled ParM (ParM stock containing 15% cy3-labeled ParM and 15% cy5-labeled ParM) was induced to polymerize by the addition of 5mM of the indicated nucleotide. Polymerization was monitored by measuring the increase in FRET signal at 690nm.

**Figure 2.**

**A) ParM polymerization in ATP.**

FRET labeled ParM at the indicated concentrations was induced to polymerize through the addition of 5mM ATP. Intensities have been zeroed to the minima of the signal.

**B) Hydrolysis dead ParM polymerization in ATP.**

FRET labeled E148A-ParM at the indicated concentrations was induced to polymerize through the addition of 5mM ATP. Intensities have been zeroed to the minima of the signal.

**C) ParM polymerization in ATP BeF<sub>3</sub>.**

FRET labeled ParM at the indicated concentrations was induced to polymerize through the addition of 5mM ATP and 2mM BeF<sub>3</sub>. Intensities have been zeroed to the minima of the signal.

**D) ParM polymerization in ATP- $\gamma$ -S.**

FRET labeled ParM at the indicated concentrations was induced to polymerize through the addition of 5mM ATP- $\gamma$ -S. Intensities have been zeroed to the minima of the signal.

**E) ParM polymerization in AMPPNP.**

FRET labeled ParM at the indicated concentrations was induced to polymerize through the addition of 5mM AMPPNP. Intensities have been zeroed to the minima of the signal.

### **F) Comparison of ParM polymerization in various nucleotides.**

15uM FRET labeled ParM to polymerize through the addition of of the indicated nucleotide. Intensities have been zeroed to the minima of the signal.

### **Figure 3.**

#### **A) Determination of the nucleus size and nucleation rate of E148A ParM.**

FRET-labeled E148A was polymerized at varying concentrations by the addition of 5mM ATP. The maximal velocity of the polymerization signal was divided by the maximal fluorescence, and the log of this value was plotted against the log of the concentration of protein. The lines in the graph have a slope proportional to  $(n - 1)$ , where  $n$  is the nucleus size, and the x intercept is the relative nucleation rate ( $k$ ). For comparison, the slopes of actin and ATP-ParM are plotted in Chapter 4 Figure 2A.

#### **B) The slow polymerization of E148A filaments can be accelerated by ParM seeds.**

Polymerized E148A (10uM) was crosslinked with EGS in an amine free buffer. The reaction was quenched with Tris-HCl, and the seeds were spun down in a TLA-100.4, resuspended in Buffer F and sheared by multiple passes through a small gage needle. The indicated volume of seeds was added to a polymerization reaction of 3uM FRET labeled E148A ParM that induced to polymerize with the addition of 2mM ATP. Polymerization was monitored by measuring the increase in FRET signal at 690nm

#### **C) ATP-BeF3 ParM polymerizes at the same rate as ATP-ParM.**

5 $\mu$ M FRET labeled ParM was combined with the indicated nucleotides and salts in a rapid mixer. Polymerization was monitored by measuring the increase in FRET signal at 690nm

**D,E) ATP “seeding” of slowly nucleating AMPPNP-ParM.**

5 $\mu$ M FRET labeled ParM was combined with the indicated nucleotides in a rapid mixer. Polymerization was monitored by measuring the increase in FRET signal at 690nm.

**Figure 4.**

**A) Nucleotide state and its effects on the FRET signal.**

FRET labeled ParM at the various concentrations was induced to polymerize through the addition of 5mM of the indicated nucleotide. For clarity only 2 concentrations of ParM are shown for each nucleotide. Intensities have been zeroed to the minima of the signal.

**B) Hydrolysis trapped forms of ParM have a FRET signal that scales differently in respect to concentration.**

The increase in FRET signal from 4A is plotted against each concentration.

**C) Combinations of nucleotides, added at different times, lead to the same final FRET signal.**

15 $\mu$ M FRET labeled ParM was polymerized with the indicated nucleotide, and at 120 seconds the second nucleotide was added.



**D) Small amounts of E148A lead to a non-stoichiometric increase in FRET signal.**

11uM of FRET labeled ParM was combined with 11uM of FRET labeled E148A at the indicated concentrations. Solutions were polymerized with 5mM ATP, and the increase in fluorescence was plotted against the percent E148A within the sample. Shown in red is the line that would be expected for a linear contribution of fluorescence from the E148A.

**Figure 5. ADP poisoning of ParM nuclei and ParR/*parC* mediated stabilization.**

**A) ADP slows down the nucleation of AMPPNP ParM.**

15uM FRET labeled ParM was induced to polymerize by the addition of nucleotide. The nucleotide was 5mM total, containing relative fractions of AMPPNP and ADP.

**B) ParR/*parC* can protect against ADP mediated destabilization of AMPPNP ParM**

20uM FRET labeled ParM was combined with the indicated amounts of ParR and *parC*, then induced to polymerize by the addition of 5uM nucleotide containing 20% ADP and 80% AMPPNP. Intensities have been normalized to the maxima and minima.

**Figure 6. Characterization of monopolar ParM tails.**

**A) Bipolar filament attachment only occurs between small *parC* coated beads.**

5uM 20% Alexa-488 labeled ParM was combined with 300nm ParR and *parC* beads of two sizes, 3um and 0.3um. The reaction was induced to polymerize by addition of 10mM ATP.

**B) Monopolar ParM tails are hollow.**

Monopolar tails were formed as in Chapter 4 Figure C. These tails were allowed to elongate for 30 minutes, and visualized using a laser scanning confocal. Shown here is a confocal slice through the center of the tail. Also shown is a corresponding intensity profile for the line shown in red.

**C) Monopolar ParM tails are composed of linear parallel protofilaments.**

Monopolar tails were formed as in Chapter 4 Figure C. These tails were allowed to elongate for 1 hour, and then visualized with a polarization microscope. The color wheel indicates the orientation of the birefringence of the sample. The constant color along the straight part of the tail indicates the filaments are aligned along the direction of motion.

**C) Monopolar ParM can push, but do not squeeze oil droplets.**

Biotinylated-cy3 labeled *parC* was combined with strepavidin and a mixture of olive oil and biotinylated lipids. This mixture was sonicated thoroughly, and the sample cleaned of free *parC* by successive washing, centrifugation, and removal of the aqueous phase. This lipid was used as a replacement for beads in the monopolar tail assay described in Chapter 4 Figure C. Shown on the left is the Alexa 488-ParM (green) and the cy3-*parC* signal (red). On the right only the Alexa 488 ParM signal.

## **Appendix A**

### **Permissions**



## License to Publish Information for Authors

A signed License to Publish must be submitted to AAAS before a manuscript can be accepted for publication in Science. Please note the following before returning your signed License:

1. This form must be signed and returned to us before your paper can be accepted for publication. We must receive either a signed hard copy, or an electronic click-through version that is available when you return your revised manuscript through our secure revision Web site.
2. Substitute forms, addenda, or changes to this form are not acceptable. Any additions or changes made to the form will delay the processing of your paper for publication.
3. Science authors grant to AAAS exclusive rights to use and authorize use of their Work, however, they retain copyright in the Work as well as rights to make certain uses of the Work. These rights are listed in the License to Publish and may be exercised by authors without any further permission from AAAS. Once the Work has been published in Science and provided the Work's first appearance in Science is properly cited, authors may:
  - Reprint the Work in print collections of the author's own writings. For example, the author may reprint the Work in a book consisting wholly of material written by the author. The Work's first appearance in Science must be properly cited. Written approval must be obtained in advance from AAAS by the author or publisher for use of the Work in publications that include works written by others.
  - Reprint the Work in print format for inclusion in a thesis or dissertation that the author writes. The author may reprint the Work, in print format, with proper credit to the Work's appearance in Science, in a thesis or dissertation written by the author as part of a course of study at an educational institution. If the thesis or dissertation is to be published in electronic format, the accepted version (the accepted version of the paper before Science's copyediting and production) of the Work should be used and a link to the Work on the Science website included.
  - Present the Work orally. The Work may be read, in full or in part in front of an audience of any size. Advance written approval must be obtained from AAAS to distribute sound recordings of any such oral presentation.
  - Reproduce the Work for use in courses the author is teaching (If the author is employed by an academic institution, that institution may also reproduce the Work for classroom use). The Work may be reproduced in photocopy format for distribution as stand-alone handouts or as part of a packet, or electronically for use by students enrolled in the course the author is teaching, with proper credit to the Work's first appearance in Science. If the author is employed by an academic institution, that institution may reproduce the Work as well, solely for classroom purposes, in either photocopy or electronic format, provided the Work is properly cited and provided that access to the Work is available only to students enrolled in courses offered by that institution.
  - Distribute photocopies of the Work to colleagues for non-commercial purposes only (providing that recipients are informed that they may not further distribute or copy the Work). Authors may distribute photocopies or download and email the Science PDF to their colleagues for their colleagues' personal use provided the recipients understand that the copy may not be further distributed or reproduced without the approval of AAAS.
  - Post a copy of the accepted version of the Work on the author's personal website. After the article has been published in Science, authors may post the accepted version (the accepted version of the paper before Science's copy-editing and production) on their personal website on the condition that the reposted article includes a hyperlink to the Work on the Science web site as well as the following notice: provided the accepted version is marked with the following notice: "This is the author's version of the work. It is posted here by permission of the AAAS for personal use, not for redistribution. The definitive version was published in SCIENCE, {VOL#}, {DATE}, doi:{nnnnn} <http://dx.doi.org/{nnnnnnn}>".

Authors may provide access to the Science version of their article from their website by taking advantage of our referrer linking service. Science provides one free referrer link per article, which enables free access to the article on Science Online, as well as the article's corresponding links, Supporting Online Material, and Science PDF. Information on this service will be emailed to the corresponding author a few days after the article has been published.

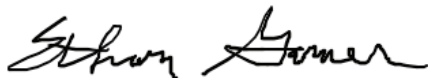
Info for authors.License to publish.2006.doc

**Publishing Agreement**

*It is the policy of the University to encourage the distribution of all theses and dissertations. Copies of all UCSF theses and dissertations will be routed to the library via the Graduate Division. The library will make all theses and dissertations accessible to the public and will preserve these to the best of their abilities, in perpetuity.*

***Please sign the following statement:***

*I hereby grant permission to the Graduate Division of the University of California, San Francisco to release copies of my thesis or dissertation to the Campus Library to provide access and preservation, in whole or in part, in perpetuity.*



\_\_\_\_\_  
Author Signature

5-15-2007

\_\_\_\_\_  
Date

**This page must be signed and dated by the author and include the correct pagination.**